The Fabrication of Photonic Bandgap Bridge Resonator Structures

by

Kuo-Yi Lim

Submitted to the Department of Electrical Engineering and Computer Science
in Partial Fulfillment of the Requirements for the Degree of
Master of Engineering in Electrical Engineering and Computer Science
at the MASSACHUSETTS INSTITUTE OF TECHNOLOGY
September 1994

Author _____
Department of Electrical Engineering and Computer Science
August 26, 1994

Certified by _____
Leslie A. Kolodziejski
Esther and Harold E. Edgerton Associate Professor of Electrical Engineering
Thesis Supervisor

Accepted by _____
Frederic R. Morgenthaler
Chairman, Department Committee on Graduate Theses

The Fabrication of Photonic Bandgap Bridge Resonator Structures

by

Kuo-Yi Lim

Submitted to the
Department of Electrical Engineering and Computer Science

August 26, 1994

In Partial Fulfillment of the Requirements for the Degree of
Master of Engineering in Electrical Engineering and Computer Science

ABSTRACT

Various forms of micromechanical bridges have been successfully built with both silicon and III-V material systems. These structures include various forms of bridges with minimum realized feature size of 1 μm and with different configurations of holes placed periodically along the length of the bridge. These structures can potentially be used to realize a new class of devices called the photonic bandgap bridge resonators. Also, micromechanical cantilevers with the smallest realized feature size of 2 μm have been constructed.

The relevant fabrication techniques used for the following material systems have been documented: (a) amorphous Si/SiO_2; (b) $GaAs/Al_{0.3}Ga_{0.7}As$; (c) GaAs/AlAs; and (d) $GaAs/In_{0.5}Ga_{0.5}P$. Specifically, the RIE and wet etch techniques for the III-V material systems have been investigated to provide a viable and reproducible fabrication process. At the same time, micromechanical issues have also been considered. For instance, stress measurements of the amorphous silicon film has been conducted. Also, important lessons are drawn from the failure of certain mechanical designs and will be instrumental in future development.

Acknowledgments

My foremost gratitude is extended to Professor Leslie Kolodziejski, whose patience, understanding and guidance have been most invaluable. She has been the mentor of my progress from a green sophomore to a (hopefully) wiser graduate student, and I don't think anyone else could have done a better job. Leslie, you are right, *science is indeed the fun part.*

This project would not have been completed without the help of Dr. Gale Petrich. His mastery of III-V MBE has provided me with playing material of such superb quality that I can have real fun in the processing labs. Above all, his friendship and advice have often shone light on matters so intuitively opaque to me.

The other students in CBE group have formed an integral part of my intellectual and social experience at M.I.T. To Jay Damask, much thanks for holding my hands at the onset of this project, particularly in the design of the mask. To Jody House, you are quite a pal and thanks for listening. Kudos to Chris Coronado, Easen Ho, Phil Fisher, Kan Lu, Joe Ahadian, and Sean Donovan: the many interesting conversations I have had with you guys have widened my realm of knowledge in more ways than I can imagine. To you all, your intellectual capacity is truly exceptional.

I would also like to thank Mari Katada, who provided the moral support so critical in keeping me on track, in both the best of times and the worst of times. Her words of encouragement helped me traveled the path I have traveled. Thank you, Mari.

My deepest gratitude is reserved for my Mom, Dad and my brothers (Kuo Kae and Kuo Fung), whose support has provided the strength in my quest for my numerous goals. Often, the subtle care half a world away does wonders.

To all my close friends, thanks for being there for me. To Paul Martin, thanks for the help with the III-V RIE. To Rich Perilli and Tim McClure, thanks for the friendly neighborhood facilities. And the catchall: to all those who have helped in one way or another, a bow to you all.

Table of Contents

List of Figures

List of Tables

Chapter 1

Introduction

Since the introduction of the concept of a photonic bandgap less than a decade ago[1,2], intense effort has been devoted to the development of the field. One of the first forays was to determine the crystal structures that would yield a photonic bandgap[3,4]. At the same time, a theoretical basis to the analysis of the structures was established where the concepts of Bloch wave functions, reciprocal space, Brillouin zones and dispersion relations became applicable[5,6]. Experimentally, photonic bandgap crystals in the lengthscale of the wavelength of operation have typically been constructed for operation in the microwave region[7,8]. At a much smaller scale, the fabrication of three dimensional photonic crystals has only been suggested[9,10] while the fabrication of a two-dimensional photonic bandgap nanostructure has recently been reported[11].

This thesis focuses on the fabrication of a class of photonic bandgap structures proposed by a group led by Professor John D. Joannopoulos at the Massachusetts Institute of Technology. These structures are essentially planar waveguides made of a high refractive index material surrounded by a medium of low index (for instance, air), with a distinct periodicity in dielectric constant along the axis of the waveguide[12] (see Figure 1.1). The waveguide itself confines electromagnetic radiation in the y and z directions, while the presence of the periodicity in refractive index along the axis results in strong confinement in the x direction. Such a structure can be physically realized by the formation of a micromechanical air bridge with holes placed periodically along the axis of the bridge.

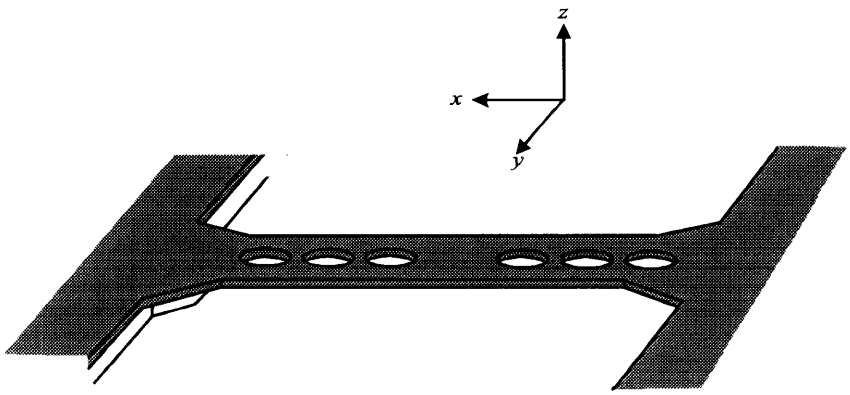

Figure 1.1: The proposed photonic bandgap bridge resonator structure.

The periodicity on the waveguide can be broken by the presence of a local defect which spatially confines electromagnetic radiation around the defect region. This defect is introduced via the removal of a single hole or by the addition of a locally different material on the bridge. A direct consequence of such a defect region is a microcavity where a high spatial concentration of a single mode electromagnetic radiation exists. Indeed, theoretical simulations of the structures have revealed the presence of a resonant defect mode with a high Q factor and compact localization[13] (see Figure 1.2).

Such a microcavity design has various important advantages over existing designs like those found in the distributed Bragg reflector (DBR) laser, the vertical cavity surface emitting laser (VCSEL) and the microdisk laser. The new microcavity design, for instance, allows for potentially very high quantum efficiencies as any spontaneous emission is channeled into a single mode. Further, the strong spatial confinement of the resonant mode implies a strong overlap of the mode with any gain region introduced in the cavity; this effect, in turn, should enhance spontaneous emissions. The high quantum efficiencies and small volume, furthermore, will vastly reduce the threshold needed to achieve spontaneous emission in the gain region. In addition, the planar configuration of the bridge structure allows for possible incorporation of large number of such structures into optoelectronic integrated circuits (OEIC), an increasingly important thrust in the research community with strong commercial appeal.

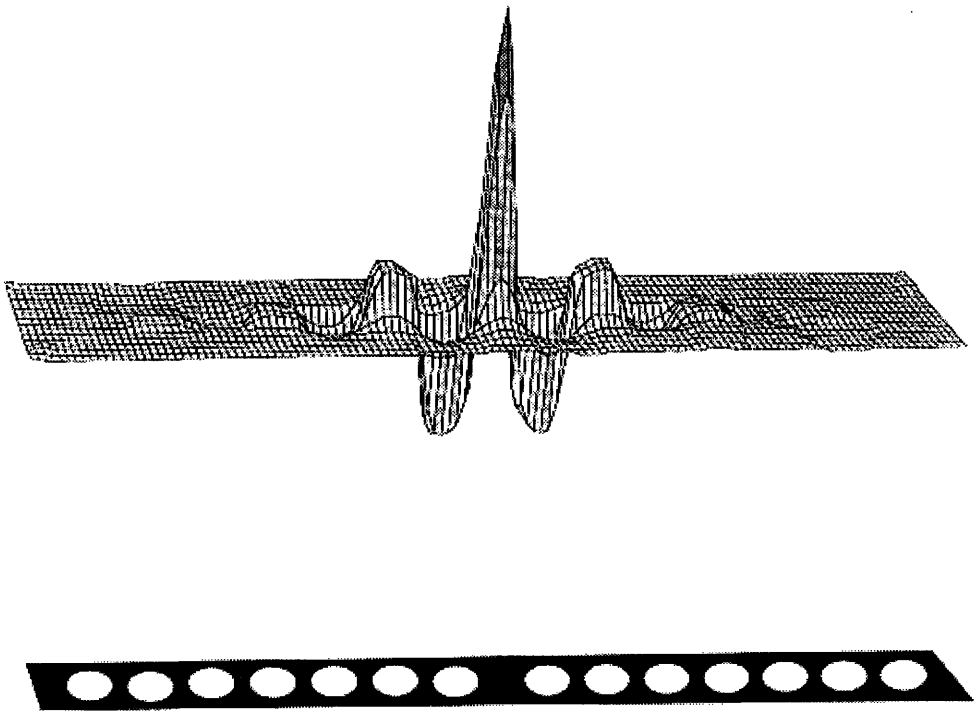

Figure 1.2: Result of computer simulations demonstrating a resonant state around the defect region using TE modes[13]. The structure at the bottom illustrates the model of an air-hole array strip waveguide that has been simulated. A defect is created by separating the otherwise periodical array of air-holes into two groups of 7 holes on both sides of the defect region. The most strongly-localized state is found at a/λ=0.24 and d=1.4a where a is the separation between holes, λ is the electromagnetic wavelength of interest, and d is the width of the defect region.

The plot at the top shows a surface plot of the z-component of the magnetic field across the waveguide. The field amplitude decays rapidly in both the x and y directions. Using the time-domain method, the Q factor of this resonant state is calculated to exceed 13,000 after an initial transient period.

The purpose of this project is to fabricate the photonic bandgap bridge structures in both Si/SiO_2 and III-V material systems. Apart from demonstrating the viability of producing these structures on the order of 1 μm in dimension, the study serves as a pathfinder in the salient issues involved in the fabrication of these micromechanical structures. In comparison, practical micromechanical structures have traditionally been constructed with Si-based materials at dimensions in the order of 10 to 100 μm. Furthermore, the fabrication of III-V micromechanical structures will be of considerable

interest since micromechanical structures using III-V materials have not been previously achieved.

The experimental techniques using silicon technology is described in Chapter 2, while those for the III-V counterpart will be documented in Chapter 3. The subsequent chapter (Chapter 4) contains a compilation of the results obtained with both material systems. Finally, the thesis closes with Chapter 5 which summarizes and outlines several possible extensions of the current work.

Chapter 2

Silicon-based Material System

While the operational photonic bandgap bridge structures will be built with III-V semiconductor material, the silicon-based approach highlights certain micromechanical issues which are also pertinent to the III-V based structures. In addition, a relatively vast amount of research knowledge and literature has already been accumulated for silicon micromechanical structures; the same cannot be said of the III-V counterpart. Consequently, an attempt to build the bridge structures with silicon technology will yield important and useful guidelines when fabricating similar III-V structures.

In this Chapter, the fabrication process for the silicon-based structures will be described in detail. The process consists of two main stages: a sequence material fabrication steps where the appropriate heterostructure is attained, and a sequence of device fabrication steps where the micromechanical structures are constructed. Further, some material characterizations deemed to provide important information are conducted and recorded.

2.1 Material Fabrication

The material system that need to be fabricated consists of a layer of SiO_2 topped with a thin film of Si (see Figure 2.1). The starting substrates for the silicon process are P-prime <100> Si wafers which are 100 mm in diameter and 525±25 μm thick. The resistivity of the wafers are specified by the manufacturers to be between 5 to 25 Ω-cm. A single lot of 25 wafers is usually used in each fabrication step.

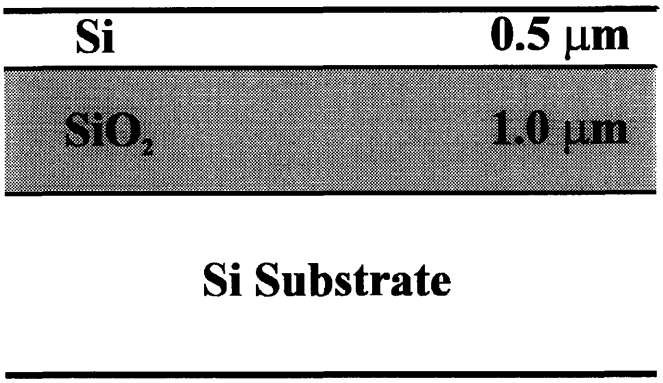

Figure 2.1: Schematic of Si/SiO_2 heterostructure.

2.1.1 RCA clean

Prior to any processing work on the wafers, an RCA clean is performed to remove any ionic or organic contaminants. The wafers are first placed in a 1:1:5 $NH_4OH:H_2O_2:H_20$ solution at 80°C for 30 minutes which removes any organic contaminants. Thereafter, the wafers are placed in a dump-rinser to rinse off the organic clean solution and then dipped in a diluted HF solution (50:1 H_2O:HF) for 15 seconds. The HF dip helps to remove the resident surface oxide and then passivates the surface[14].

After the HF dip, the wafers are rinsed and placed subsequently in an ionic clean solution of 6:1:1 $H_20:HCl:H_2O_2$ which has already been preheated to 80°C. Following a 30 minute clean in the solution, the wafers are again rinsed in a dump-rinser. Finally, the wafers are spun dry in a spin rinser/dryer.

2.1.2 Low-Temperature Oxide (LTO) Deposition

The sacrificial layer is made of SiO_2 deposited at low temperature which is highly amenable to removal by wet chemical etch. A 1.0 μm layer of LTO is deposited by low-pressure chemical vapor deposition (LPCVD) in the Integrated Circuit Laboratory (ICL) of the Microsystems Technology Laboratory (MTL) at M.I.T. The deposition is performed in an automated Heraeus Amerasil Model SLS-125 furnace. The deposition temperature is 400°C and the gas flow rates are: 30 sccm N_2, 31 sccm O_2 and 38.5 sccm SiH_4.

2.1.3 Amorphous Silicon Deposition

The thin film that will ultimately form the beam of the bridges is made of amorphous silicon. An amorphous silicon deposition is performed in the LPCVD furnace at the Teaching Research Laboratory (TRL) in MTL. At a system pressure of 150 mTorr, a SiH_4 flow rate of 60 sccm, a N_2 flow rate of 240 sccm and a deposition temperature of 590°C, the expected deposition rate is approximately 2000 Å/hour. Unlike the LTO deposition, LPCVD of the amorphous silicon is done manually where wafers are loaded onto a short quartz boat and then gradually introduced into the furnace with a quartz rod.

In all the experiments conducted for the silicon-based system, 5000 Å of amorphous silicon are deposited. In addition to the actual wafers that are used in fabricating the bridge structures, monitor wafers with an existing layer of SiO_2 1000 Å in thickness are included with the batch.

2.1.4 Thickness Measurement

The actual thickness deposited after each deposition step above invariably deviates from the initial targeted thickness. This is due to fluctuations in process parameters which are beyond the control of the operator. For instance, the temperature along the quartz wafer boats varies with distance away from the furnace door, hence resulting in non-uniform film thickness across the entire lot of wafers. Consequently, monitor wafers are used to measure the actual thickness of the films grown with the use of an ellipsometer.

In the LTO deposition, the average thickness is measured on the process wafers to be 9900±100 Å. The wafers further away from the furnace door are found to possess thicker but more non-uniform films. In the amorphous silicon deposition, the thickness measurement is performed on the monitor wafers since the ellipsometer is already programmed to measure the thickness of silicon films on 1000 Å thick SiO_2*. The

---

* The reflectivity of a silicon film on 1 μm thick SiO_2 is unknown and to use an actual wafer for the thickness measurement would require additional calibration. As such, monitor wafers with 1000 Å of SiO_2 are used in anticipation of the limitations of the ellipsometer.

amorphous silicon film thickness after 2½ hours of deposition is measured to be 5500±75 Å. Unlike the oxide deposition step, there is no discernible pattern in the variation of film thickness between wafers in any single lot. This is probably due to the fact that the quartz boat used is short and the total number of wafers involved in the deposition was only 8 (in contrast, 25 wafers were used in the oxide deposition step). Consequently, the wafers are not placed sufficiently far apart for a systematic variation to be discernible.

2.1.5 Stress Measurement

At the early stages of the project, a polysilicon thin film deposited by LPCVD at 630°C has been used in place of the amorphous silicon layer. However, the residual stress in the polysilicon layer is found to be highly compressive in nature[15]. Consequently, any bridges constructed from this film are found to twist and buckle. Such a phenomenon was indeed observed in one of the first attempts at the bridge construction and is demonstrated in Figure 2.2.

The solution is found in several studies conducted on the nature of stress in polysilicon films deposited under different growth conditions[16,17]. In particular, the studies revealed that silicon deposited within a certain temperature range will result in a thin film with residual tensile stress. The temperature range that will produce a tensile film for a particular LPCVD furnace depends largely on the system pressure at which the film is deposited. Further, rapid thermal annealing of the samples after the silicon deposition will often release or eradicate any form of stress in the film.

To attain bridges that are less likely to buckle, therefore, the thin film forming the beams should have ideally zero or low tensile stress*. In the TRL, for instance, the amorphous silicon deposition recipe at 590°C was established to yield a tensile film[18]. To confirm this supposition, the residual stresses in the amorphous silicon films deposited for this project are measured.

---

* High tensile stress, on the other hand, may be undesirable since the film may rip under the stress.

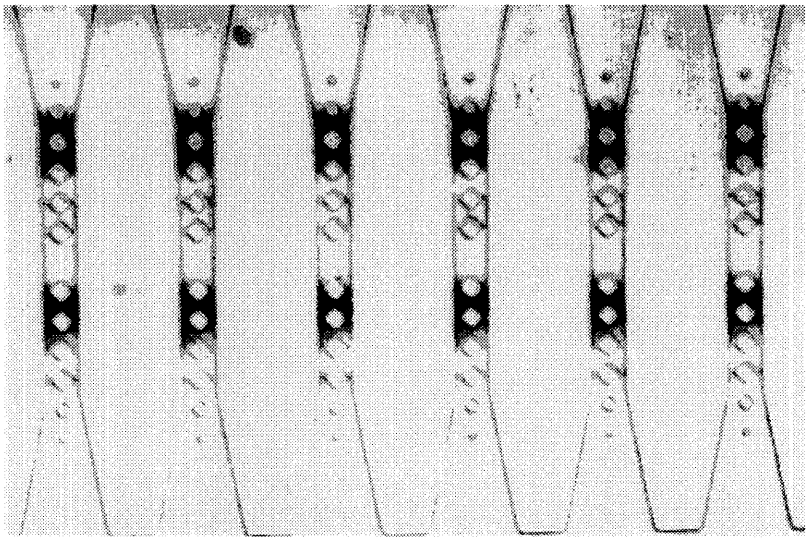

Figure 2.2: (Plan view) Nomarski microscope photograph of a photonic bandgap bridge structure using polysilicon as the bridge material. Note the alternating bright and dark fringes which correspond to the difference in the depth of focus at various parts of the beam. This phenomenon is due to the buckling of the beam, which in turn arises from the compressive nature of the film.

The stress measurements are achieved with a TENCOR FLX-2320 Stress Measurement Instrument on three wafers chosen from different positions of the quartz boat. The measurement technique is based essentially on the change in wafer curvature that results from the deposition of an additional film on the surface. The radius of curvature of the wafer is determined by a laser beam which scans across the diameter of the wafer parallel to the flat. A first scan is made on the wafer before the film deposition. After the subsequent film deposition, the wafer is reintroduced into the equipment and the surface curvature measurement is repeated. By setting the wafer on a customized block, it is ensured that the laser beam will scan the same location on the wafer as the first scan. The difference in curvature before and after the film deposition is calculated and provides a notion of the nature of the stress inherent in the film. For instance, the stress is tensile if the surface of the wafer is concave, compressive if convex (see Figure 2.3)[19].

Quantification of the stress is provided by the following equation[20]:

$$\sigma_f = \frac{E_s t_s^2}{6(1-\upsilon_s)t_f R_c} \qquad \text{(Eq. 1)}$$

where the symbols represent the following:

σ_f: stress of the deposited film
t_f: thickness of the deposited film
E_s: Young's modulus of the substrate
t_s: thickness of the substrate
ν_s: Poisson's ratio of the substrate
$\frac{E_s}{(1-\nu_s)}$: biaxial Young's modulus of the substrate

In the calculations, a (100)Si substrate, instead of the actual SiO_2, is assumed to be underneath the amorphous silicon film. Consequently, the biaxial elastic modulus of (100)Si is used. This assumption is valid since the thickness of the oxide deposited (1 μm) is negligible compared to the substrate thickness (525 μm). As such, the deposited amorphous silicon film can be considered to be effectively changing the radius of curvature of the silicon bulk. The parameters used in the calculations and the results are given in Table 2-1. The results confirm that the amorphous silicon film is indeed tensile in nature.

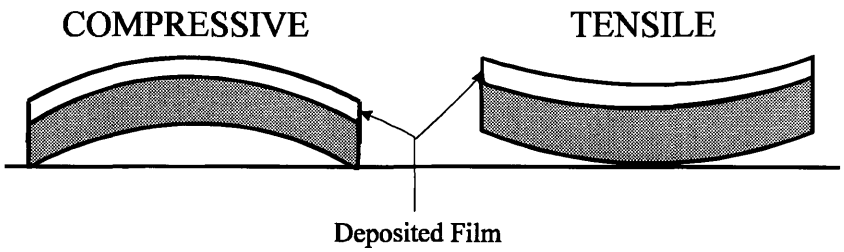

Figure 2.3: Types of residual stress within deposited film.

Biaxial Young's Modulus, $\frac{E_s}{(1-\nu_s)}$	1.805×10^{11} Pa
Film thickness, t_f	0.5 μm
Substrate thickness, t_s	525 μm
Substrate type	(100) Si
Substrate Diameter	100 mm
Stress of Amor. Si Film #1*	+179.9 MPa
Stress of Amor. Si Film #2	+213.2 MPa
Stress of Amor. Si Film #3	+205.3 MPa
Average Stress	+200 MPa

Table 2-1: Parameters used in the stress measurement of the amorphous silicon film with the TENCOR FLX 2320.

2.2 Device Fabrication

2.2.1 Process Outline

The fabrication process for both silicon and III-V material systems are identical and is illustrated by Figure 2.4. The first step in the process involves the photolithography and pattern definition of the bridges. A sequence of reactive-ion etching follows that will cut anisotropically into the material and expose the sacrificial layer to the subsequent wet etch. The bridges are then released from the underlying sacrificial material by a selective wet etch.

* The residual stress is tensile if the stress value is positive, compressive if negative.

2.2.2 Mask design

The mask consists of various micromechanical structures of varying dimensions. The smallest feature on the mask has the dimension of 0.5 μm which pushes the limit of optical lithography. The mix of structures is conceived to reveal as much information pertaining to micromechanical issues as possible. The structures include cantilevers of different lengths and widths, bridges with and without periodic holes, and bridge structures corresponding to a design suggested elsewhere[21]. A layout and explanation of the mask design can be found in Appendix A. The same mask design is used in both the Si/SiO_2 and III-V processes.

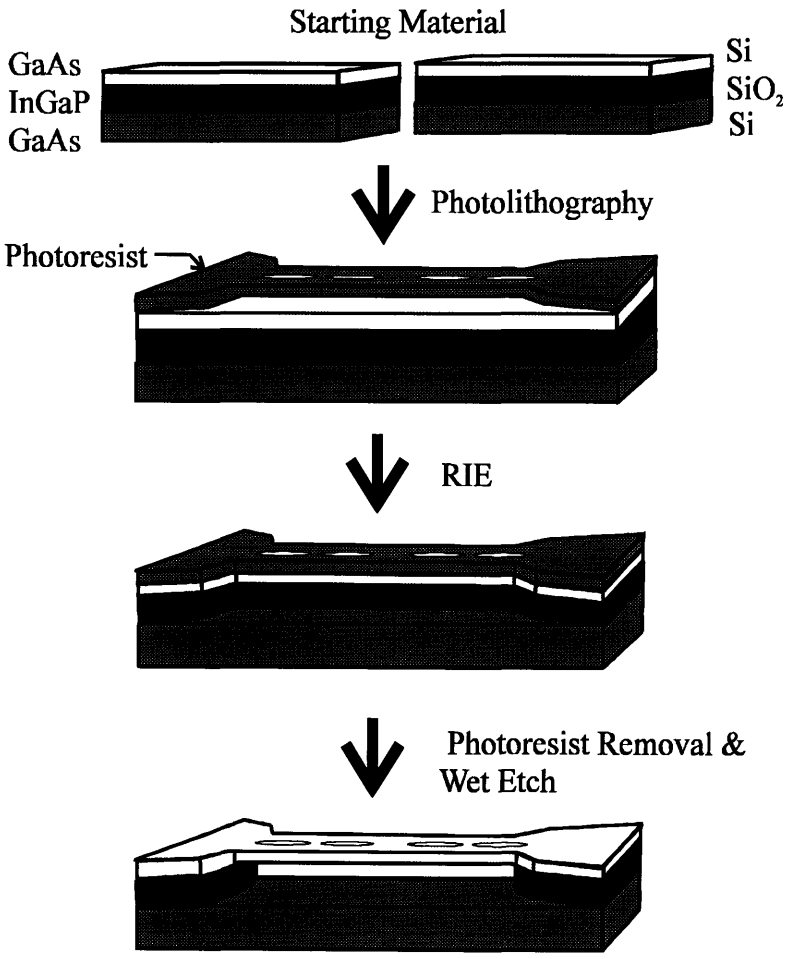

Figure 2.4: An illustration of the process outline for the fabrication of the photonic bandgap bridge resonator structures. Apart from InGaP, the sacrificial layer for the III-V material system has also been made from $Al_xGa_{1-x}As$ where x=0.3 or 1.0.

2.2.3 Photolithography

The photolithography step is probably the most critical of all the fabrication steps involved in this project. In particular, the definition of minimum feature sizes of 1 μm, which pushes the efficacy of optical lithography, requires care, practice and patience. Iterations and rework are not uncommon in establishing the acceptable photolithographic results before proceeding to the next step. Once the subsequent processing steps have been committed, a dissatisfactory lithography outcome will be irreversible.

The Si wafers are first vapor-coated with hexamethyldisilazane (HMDS) to improve the photoresist adhesiveness on the surfaces. The treated wafers are then batch processed on a GCA Wafertrac 1006 spin coater where they are first subjected to a dehydration bake at 200°C. After the brief pre-bake, OCG 820-27CS positive photoresist is then spun onto the wafers at 5000 rpm for 20 s (with an initial dynamic dispense). The resulting photoresist thickness on a flat surface is specified by the ICL to be 1.15 μm. The coated wafers are then soft-baked for 30 s at 130°C. The pattern transfer is performed with a stepper using a 10X reticule printing out an array of 10-by-10 dies on the wafer. The printed wafers are then brought back to the Wafertrac 1006 where the wafers are developed with the OCG934 developer. The photolithography step is completed after a post-bake of 30 s at 130°C.

An initial focus-exposure characterization is usually conducted by varying the focus and exposure parameters on the stepper across a test wafer, hence creating a matrix of patterns formed with different focus depth and exposure times. A careful visual examination of the so-called "focus-expo" wafer is then carried out with an optical microscope. The pattern that appears to be the most sharply focused and well exposed is selected and provides the focus depth and exposure time to be used for the actual process wafers.

To facilitate the task of deciding the best focus depth and exposure time, special patterns have been included on the mask. In particular, the desired focus can be determined by comparing the mask objects which appear as both dark field and bright field patterns. For instance, the features in Figure 2.5 should all have the same width if the focus is adequate. To decide if a certain exposure time is satisfactory, one would look at the array of squares as illustrated in Figure 2.6. The coloration observed within the squares provides a good indication of whether the photoresist has been exposed to the right extent. Specifically, a pink coloration due to the photoresist will remain within the square patterns which have not been sufficiently exposed. In addition, the squares provide

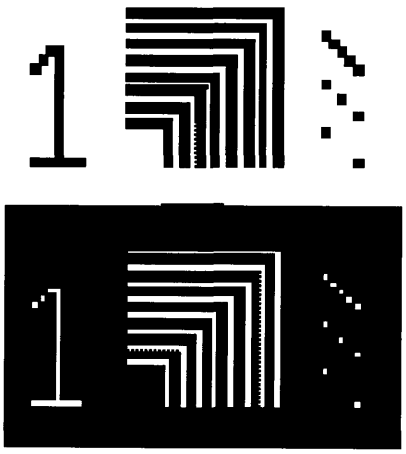

Figure 2.5: Special markers used for achieving the best depth of focus and exposure time.

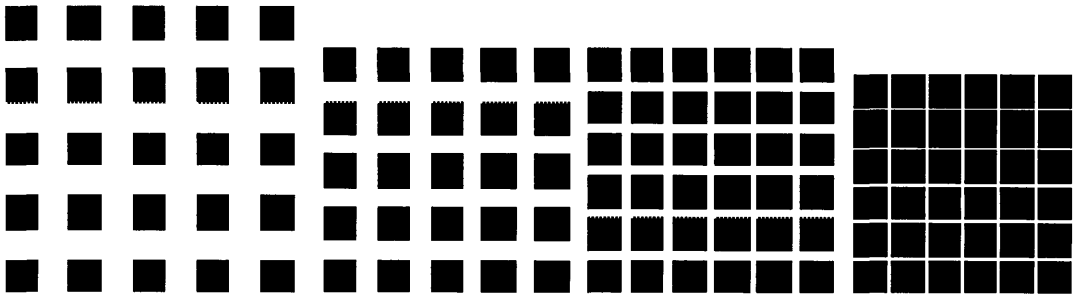

Figure 2.6: A series of squares useful in determining the limits of resolution and adequacy of exposure.

a gauge of the resolution limits in the lithography technique by determining the smallest squares and square separation with the highest pattern fidelity.

Upon reaching a subjective decision on the focus depth and exposure time that yields the best results, the actual process wafers are processed with the stepper set at the particular focus-exposure combination. A brief visual inspection is usually performed on the first wafer that has been exposed with the set values before committing the entire lot to the process. In the event that the outcome of the photolithography is not satisfactory in any way, the photoresist can be removed by a photoresist asher and the entire step repeated.

2.2.4 Reactive Ion Etch

The technique of reactive ion etch (RIE) has the important property of achieving good anisotropy of the etched features. Consequently, the method is ideal in defining the vertical walls of the micromechanical bridge structures. In this project, the two layers of top semiconductor materials will be etched anisotropically by RIE, hence exposing the sacrificial layer for the subsequent wet chemical etch.

Two separate parallel-plate, fully automated LAM Research AutoEtch 690 systems are used for the RIE steps. For the amorphous silicon layer, a gas mixture of CCl_4/O_2 in a He ambient is used. The gas flow rates are, respectively, 130 sccm for CCl_4, 20 sccm for O_2 and 70 sccm for He. The system pressure is set at 200 mTorr and an

incident power of 300 W is used. The samples are etched until a preset endpoint has been reached.

Subsequently, a gas mixture of CHF_3, CF_4 and O_2 in a N_2/He ambient is used to etch the underlying LTO layer. The etch parameters are set at gas flow rates of 30 sccm for CHF_3, 130 sccm for CF_4, 5 sccm for O_2, 125 sccm for He, 30 sccm for N_2, system pressure of 3 torr, and incident power of 900 W. The samples are etched for 1 minute 40 seconds at an etch rate estimated to be 50 Å/second, followed by an overetch of 20 seconds with the following settings: system pressure of 2 torr, incident power of 800 W, and gas flow rates of 10 sccm for CHF_3, 60 sccm for He and 5 sccm for O_2.

It has been observed that apart from the semiconductor material, the photoresist has also been marginally etched during the RIE steps. Consequently, some of the smallest hole patterns have been enlarged to merge with the sides of the bridges. After the sacrificial layer is removed with the subsequent wet etch, these bridges are seen to be in a state of collapse and destruction (see Figure 2.7). In a satisfactory photolithography step, the smallest holes that survive the RIE steps are 2 μm in diameter. This observation provides an indication of the resolution limits of the stepper in the ICL.

The remnant photoresist on the wafers is then stripped in a DryTek Megastrip 6 H.F. asher using an O_2 plasma with a setting of 950 W incident power and 400 mTorr

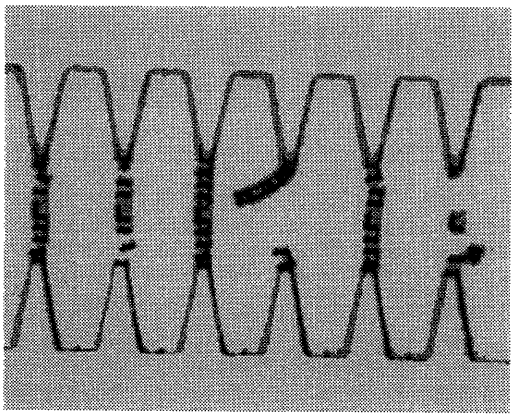

Figure 2.7: (Plan view) Nomarski microscope photograph (cropped and magnified) showing collapsed and broken bridge structures (4 μm wide with 2 μm diameter holes). The difficulty in obtaining a sharp focus from the photolithography and the subsequent degradation of the resist by the RIE steps cause the holes to enlarge and merge with the edges.

system pressure for about 15 minutes.

2.2.5 Wet Etch

The purpose of the wet etch step is to remove the sacrificial layer supporting the bridges. By choosing a chemical system that will selectively etch LTO over silicon, the beams that form the bridges will ideally be unscathed and the bridges thus formed should be free-standing. Apart from the etchant selectivity between LTO and Si, the etch should also be isotropic so that there is appreciable undercutting of the beams to free the bridges. In this particular instance of LTO and Si, hydrofluoric acid (HF) presents a highly effective etchant for the purpose.

Before the wet etch step, the array of 10x10 dies is first cut into individual dies with a die-saw outside the ICL. The dies are then brought over to the Chemical Beam Epitaxy (CBE) Laboratory where the wet etch is performed. Each individual die, held by a teflon tweezer, is carefully dipped in a teflon petri dish containing concentrated (49%) HF. The etching action is fairly rigorous as bubbles can be seen forming on the surface of the die.

After a period of 20 minutes, the die is removed and rinsed twice in two petri dishes of deionized water. Finally, the die is rinsed with isopropanol and left to dry in the acid hood. The use of isopropanol essentially dehydrates the material. At the same time, isopropanol has a lower surface tension than water or other commonly available alcohol. This is particularly relevant since a high surface tension of the rinsing liquid may pull the beams down as the liquid evaporates and shrinks (see Figure 2.8). When the beams are

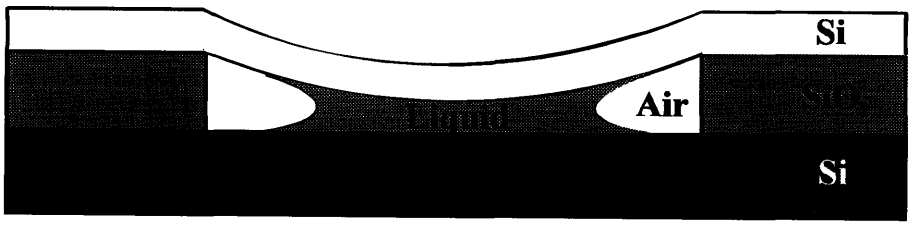

Figure 2.8: Surface tension of the drying liquid meniscus pulling the beam down.

pulled down and come into contact with the substrate surface, the stiction force between the two entities may cause the top layer to be permanently pinned to the substrate[22].

A novel method employed to circumvent the problem posed by the surface tension of the rinsing agent is called the freeze-drying technique[23,24]. In one variant of this method, tertiary butyl-alcohol (tert-butyl alcohol) is used. Tert-butyl alcohol has the unique property of having a melting point at 25°C and remaining in solid form at room temperature. The sample is first dehydrated by a isopropanol rinse followed by an immersion in the tert-butyl alcohol that has been melted on a hotplate. The container of liquid alcohol together with the sample is next placed in a freezer where the alcohol readily freezes. The container is subsequently transferred to a vacuum chamber which is then evacuated. As the pressure in the chamber decreases, the alcohol will sublimate (i.e. changes from solid to gaseous phase without passing through the liquid phase). Consequently, the problem that would have arisen from any liquid surface tension will thus be avoided.*

Even though experiments employing the technique have been conducted, the technique is found to be largely unnecessary for the purpose of the project. This is due to the fact that the tensile residual stress in the film itself is sufficiently large to render the downward pulling action of the drying liquid irrelevant. Nonetheless, the freeze-drying technique remains a valuable procedure that could prove useful in the future.

---

* The sublimated tert-butyl alcohol that has been evacuated from the vacuum chamber may condense in the pump. The alcohol is known to degrade the pump oil that is routinely used in most pumps. As such, as small an amount of alcohol should be used or frequent replacement of the pump oil may be necessary.

Chapter 3

III-V Material System

3.1 Material Fabrication

a. Gas Source Molecular Beam Epitaxy (GSMBE)

The III-V heterostructures are fabricated using the technique of GSMBE in the Chemical Beam Epitaxy Laboratory. The crystal growth is performed in a Riber CBE 32P reactor, a system which has been described elsewhere[25,26]. The starting substrates consist of one-quarters of epitaxy-ready 2-inch GaAs wafers mounted with melted indium solder on 3-inch silicon wafers. Prior to each growth, the native oxide on the substrate is desorbed and the flux of the material sources measured. During the growth, an InSb eutectic mounted near the samples together with a pyrometer are used to calibrate the temperature reading of the thermocouple located close to the substrate. Further, Reflection High Energy Electron Diffraction (RHEED) oscillations off the surface of the sample are used to measure the real-time growth rates. Detailed description of the growth procedures can be found in references 25 and 26.

The typical structure fabricated for the purpose of this project is illustrated in Figure 3.1. The top GaAs layer represents the material that forms the beam of the micromechanical structures and is chosen for its relatively higher dielectric constant at a wavelength of 1.55 μm. The sacrificial layer is made of either $In_{0.5}Ga_{0.5}P$, $Al_{0.3}Ga_{0.7}As$ or AlAs, which also form the supports on either end of the GaAs beam. The choice of the sacrificial material is based primarily on the presence of an effective selective etch between GaAs and the sacrificial layer material. The refractive index differential between the two materials should also be as large as possible. In addition, the various layers are

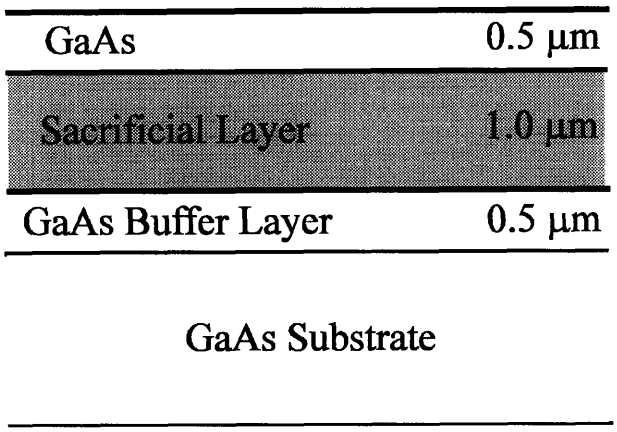

Figure 3.1: Schematic of III-V heterostructure.

lattice-matched to provide an essentially stress-free top film, which enhances the mechanical stability of the micromechanical structures.

The thickness of the top two layers are chosen arbitrarily, though the beam should be as far above the substrate as possible. However, the maximum practical thickness is limited by the GSMBE growth of the material in the system. A thickness of 1 μm is chosen as a reasonable thickness for both growth and device performance. Directly underneath the sacrificial layer and on top of the substrate surface is a GaAs buffer layer which is 0.5 μm thick.

For the GaAs/$In_{0.5}Ga_{0.5}P$ heterostructure, the GaAs buffer layer is first epitaxially grown at a rate of 0.46 μm/hour as deduced from the RHEED oscillations. During the process, the substrate temperature is maintained at 590 °C, with the Ga source at 880 °C and the arsine cracker temperature at 900 °C. The As flux is measured to be 1.00 sccm. The $In_{0.5}Ga_{0.5}P$ layer is grown at a rate of 0.89 μm/hour with the substrate temperature at 470 °C, the Ga source at 880 °C, the In source at 790 °C and the arsine cracker at 900 °C. The As flux is calculated to be 2.00 sccm while the mole fraction is estimated to be 51.5% Ga. A few monolayers of GaAs is next grown at a substrate temperature of 470 °C with all other settings identical to those used for the buffer layer. Finally, the top GaAs layer is grown using the same parameters as the buffer layer.

For the GaAs/$Al_{0.3}Ga_{0.7}As$ heterostructure, the GaAs buffer layer is epitaxially grown with the substrate at 620 °C, the Ga source at 910 °C and the arsine cracker at 900 °C (resulting in an As flux of 1.00 sccm). The growth rate is calculated to be 0.74 μm/hour. The $Al_{0.3}Ga_{0.7}As$ layer is grown at a rate of 1.05 μm/hour, with the substrate at 620 °C, the Ga source at 910 °C, the Al source at 1070 °C and the arsine cracker at 900 °C (As flux=1.00 sccm). The final top GaAs layer is grown at the same conditions as the buffer layer.

For the GaAs/AlAs heterostructure, the GaAs buffer layer is grown with the substrate temperature set at 620 °C, the Ga source at 930 °C and the cracker at 900 °C (As flux=1.00 sccm). The AlAs layer is grown with a substrate temperature of 620 °C and the Ga source at 930 °C , the Al source at 1090 °C and the cracker at 900 °C (As flux=1.00 sccm). The growth rate is estimated from RHEED oscillations to be 0.50 μm/hour. Finally, the top GaAs layer is grown at the same conditions as the initial GaAs buffer layer.

b. Sample Dismount and Backside Indium Removal

After the heterostructures have been fabricated and removed from the GSMBE reactor, the quarter wafers need to be dismounted from the 3-inch silicon wafer for further processing. The indium solder which mounts the quarter wafers onto the silicon wafer is first melted by placing the silicon wafer on a hot plate. The quarter wafers are then carefully removed by a sliding action along the silicon wafer, leaving behind as much indium as possible.

At this juncture, a considerable amount of indium is still left on the back of the quarter wafers. The roughness that results from the remnant indium solder will render processing of the samples difficult, hence as much of the so-called backside indium should be removed as possible. This is achieved by first mounting the sample with its face down on a glass slide with wax. The glass slide is then introduced into a concentrated hydrochloric acid (HCl) solution. Since HCl will also etch GaAs, the surface is protected

from the etchant by ensuring that the wax has fully sealed the edges of the wafer while not covering any of the backside indium.

Upon dipping the backward-mounted sample in the HCl, rigorous reaction can be observed as the acid begins to etch the remaining indium. After a period of about 30 minutes, most of the indium will have been removed. Note that it is not entirely possible to remove all the remnant indium solder, and some roughness will remain. But the back of the sample should be fairly smooth after the etching action has subsided.

The wax used to mount the sample on the glass slide will next be removed. The glass slide is placed in a beaker of boiling 1,1,1-trichloroethane (TCA) which dissolves the wax. The sample is then transferred to another beaker of boiling TCA, spraying the surface with TCA and keeping it covered with the solvent during the transfer. Care should be taken not to allow the TCA to dry up at any point, as this may leave some particularly stubborn wax residue on the sample. The sample is finally rinsed in acetone followed by methanol, and then dried with a stream of nitrogen. Visual inspection of the sample surface while the methanol is evaporating will give a good indication of its smoothness and the amount of residue that may have remained.

3.2 Device Fabrication

Fabrication of the III-V material-based devices is performed in the Microelectronic Technology Central Facility (MTCF) at the Center for Material Science and Engineering. The environmental control of the MTCF is considerably less stringent than the ICL. In addition, a variety of material research is conducted in the Facility, in contrast to the ICL where only silicon-based materials are allowed.

3.2.1 Photolithography

The sample is first prebaked in a 200°C oven to remove any moisture from the surface and hence to improve the adhesiveness of the photoresist. Immediately upon its removal from the prebake oven, the sample is spin-coated with photoresist. The photoresist used is the Shipley 1400-27 positive resist, which is statically dispensed onto the sample with a

filtered syringe. The sample is then spun at 5000 rpm for 30 seconds which yields an average photoresist thickness of 1.15 μm. A soft bake at 90°C for 30 minutes follows the spin-on step.

After the soft bake, the sample is allowed to cool to ambient temperature. Exposure with a one-step contact mask is then performed on a Karl Suss aligner with the wavelength set at 320 nm and the incident power of 8 mW/cm^2. Unlike in the ICL, the aligner is set manually and the focus deemed sufficient is purely subjective. After an exposure time of 39 seconds, the sample is developed in the Shipley MF319 resist developer for 75 seconds, followed by a rinse in a beaker of deionized water for a minute. Visual inspection on a microscope is then carried out to ensure that the pattern transfer is satisfactory. The technique used to decide if the optical focus and exposure time are adequate is as described in Section 2.2.3*. In addition, a monitor GaAs wafer is usually used together with the actual samples to confirm the process values. The samples are finally hard-baked at 130°C for 30 minutes.

3.2.2 Reactive Ion Etch

The technique of RIE has traditionally been of great interest in III-V material processing, particularly since mesa definition forms the usual approach in III-V device fabrication. Not only does RIE yield an etch profile with higher anisotropy and resolution than wet etching, it also allows a more controlled etch rate. As such, great attention has been paid to the development of RIE processes for various combinations of III-V heterostructures.

The types of gases used in the RIE of III-V materials can basically be classified into two main categories[27]. One is the chlorine- or bromine-based gas mixtures which are effective since gallium and most other group III chlorides or bromides are volatile at low temperatures. Indium-based III-V materials, however, form the major exception to this

---

* Note that the exposure and development times have been determined by a previous characterization exercise with plain GaAs wafers. In that experiment, different exposure and development times are explored to yield the most satisfactory parameters.

rule as the indium chloride by-products are reported to have low vapor pressure[28] and tend to leave an undesirable residue on the etched surface. The other main category of gases consists of the methane or ethane and hydrogen mixtures. These gas mixtures have been reported to etch both gallium- and indium-based material[29,30]. The main difference of using the organic gases lies in the fact that the etch rate for GaAs is notably lower than that with the chlorine-based gases.

In this project, three different III-V heterostructures are used, namely (a) GaAs/$In_{0.5}Ga_{0.5}P$; (b) GaAs/$Al_{0.3}Ga_{0.7}As$; and (c) GaAs/AlAs. All the samples are etched in a PlasmaTherm 700 Series PECVD*/RIE system at the MTCF. The system consists of a set of parallel plate electrodes driven at an RF frequency of 13.56 MHz tuned with an automatic impedance matching network. The temperatures of the lower electrode and the chamber walls are controlled via a heat exchanger and the system is evacuated to high vacuum with a turbomolecular pump.

In the experiments, the samples consist of single dies which have been cleaved from the quarter wafers after the photolithography step. Prior to the initial use of the system, the RIE chamber is usually cleaned with O_2 plasma using a standard recipe in the MTCF.

For the GaAs/ $In_{0.5}Ga_{0.5}P$ heterostructure, the RIE procedure involves a sequence of etches using gases from both categories described above. The first etch involves the $SiCl_4/BCl_3$ gas mixture which removes most of the top GaAs layer. The flow rates for the gases are 20 sccm for $SiCl_4$ and 30 sccm for BCl_3, while the system pressure is set at 15 mTorr. The temperatures of both the chamber walls and the lower electrode are kept at 40°C using a heat exchanger, and a DC bias of -300 V is employed. In addition, an alumina susceptor is used to protect the lower electrode from the corrosive chloride gases. The sample is etched for 1 minute 48 seconds with an expected etch rate of about

---

* PECVD is the acronym for Plasma Enhanced Chemical Vapor Deposition.

2500 Å/min*, hence leaving about 500 Å of GaAs before the GaAs/ $In_{0.5}Ga_{0.5}P$ interface. The etch time is chosen such that the $In_{0.5}Ga_{0.5}P$ layer will not be exposed to the $SiCl_4/BCl_3$ gas. At the same time, as much of the GaAs is etched away as possible since the next gas mixture (CH_4/H_2) etches GaAs very slowly.

At this juncture, a brief O_2 plasma clean is performed to remove any residual $SiCl_4$ or BCl_3 gases that might have remained in the chamber. The settings for the system for the clean step are: gas flow rate of 100 sccm, system pressure of 75 mTorr, incident power of 100 W and active plasma discharge time of 10 minutes. The rest of the GaAs layer and about 2000 Å of the $In_{0.5}Ga_{0.5}P$ layer are then etched with the CH_4/H_2 mixture using the following parameters: gas flow rates of 10 sccm for CH_4 and 40 sccm for H_2, system pressure of 20 mTorr, DC bias of -300 V and etch time of 20 minutes. The temperatures of the chamber wall and the lower electrode are both raised to 50°C. The sample is placed on a cleaned silicon wafer (on top of the alumina susceptor) to reduce the residue that tends to appear after the etch. In fact, the residue on the sample surface is further removed by a O_2 plasma etch with 100 sccm gas flow rate, 200 mTorr system pressure and 100 W incident RF power for 5 minutes after the CH_4/H_2 etch.

For both the GaAs/$Al_{0.3}Ga_{0.7}As$ and GaAs/AlAs heterostructures, only the single gas mixture of $SiCl_4/BCl_3$ is used with the same parameters as in the case of the GaAs/$In_{0.5}Ga_{0.5}P$ structure. The etch times for both structures are 4 minutes and the top layer of GaAs is completely etched away together with about 3000 Å of $Al_{0.3}Ga_{0.7}As$ and 3600 Å of AlAs. Finally, the bulk of photoresist remaining on the samples is removed by spraying the sample first with a stream of acetone, followed by methanol. A 5-minute O_2 plasma ash at 100 W incident RF power, 100 sccm gas flow rate on an asher removes any remaining photoresist residue.

---

* See Appendix B for a detailed calculation of the etch rate for the various RIE experiments conducted for this project.

3.2.3 Wet Etch

One of the main criteria for the heterostructures to use for this project is the existence of a highly selective etch between the bridge material and the sacrificial layers. In the case of the GaAs/$Al_xGa_{1-x}As$-based material systems, a host of effective selective wet etches between the two materials have long existed. The various etching solutions that etch $Al_xGa_{1-x}As$ selectively over GaAs include: (a) a hydrogen peroxide/ammonium hydroxide (H_2O_2/NH_4OH) mixture; (b) a ferrichloride/ferrochloride ($FeCl_3/FeCl_2$) mixture; (c) a potassium ferricyanide/potassium ferrocyanide [$K_3Fe(CN)_6/K_4Fe(CN)_6$] mixture; (d) a cerium IV sulfate/cerium III nitrate [$Ce(SO_4)_2/Ce(NO_3)_3$] mixture; (e) a iodine/potassium iodide (I_2/KI) mixture; and (f) hydrofluoric acid (HF).

Of the mixtures above, etchant (a) involves chemicals that are readily available in electronic grade purity but require a tight pH margin for the solution to selectively etch $Al_xGa_{1-x}As$[31]. Etchants (b), (c) and (d) also involves stringent pH requirements for the selective etch to be effective[32], and the chemicals are relatively more expensive in their purer forms. Etchant (e) is stable over a wider range of pH but still requires a chemical which is costly in a sufficiently pure form. Nonetheless, the I_2/KI mixture has shown good selectivity and etch rates[32]. Etchant (f) has also demonstrated good etch rate and selectivity, but the etch rate at room temperature becomes grossly inadequate when the aluminum content in the alloy is less than 40%[33]. To achieve appreciable etch rate for $x<0.40$ in the $Al_xGa_{1-x}As$ alloy, the HF solution needs to be heated which causes the emission of an undesirable and dangerous fume.

For the purpose of this project, the HF etching solution was used for both the GaAs/$Al_{0.3}Ga_{0.7}As$ and GaAs/AlAs heterostructures. For the former, the sample is etched in a teflon petri dish where warm 49% concentrated HF solution is added periodically. The HF solution is warmed in a PFA beaker which is, in turn, placed in a warm water bath kept at 60°C. Since the HF solution begins to fume at about 40-50°C, the experiments are

conducted in a well-ventilated acid hood*. For the GaAs/AlAs heterostructures, the samples are readily etched in a HF solution at room temperature. In fact, the etching of AlAs is so rigorous in an undiluted HF solution that a mixture of 20:1 H_2O:HF is preferred. Even for this amount of dilution, the AlAs material is sufficiently undercut such that the sacrificial layer is removed after 30 seconds with discernible bubbling in the process. For both etches, two rounds of rinsing in two separate petri dishes of deionized water ensue. The sample is finally rinsed in isopropanol and left to dry in the hood.

In contrast to the GaAs/$Al_xGa_{1-x}As$ heterostructures, significantly less work has been published about the selective etching of $In_{0.5}Ga_{0.5}P$ over GaAs. The main etching solution that has been reported to date is the H_3PO_4/HCl/H_2O mixture which demonstrates good selectivity and etch rate, as well as little surface roughness after the etch[34]. In the experiments for this project, several etching solutions with different proportions have been used with varying results (see Appendix B). These solutions include a 1:1:5 H_3PO_4/HCl/H_2O solution, a 1:1 H_3PO_4/HCl solution, a 1:4 H_3PO_4/HCl solution and a 1:10 H_3PO_4/HCl solution. All of the GaAs/ $In_{0.5}Ga_{0.5}P$ selective wet etches are conducted at room temperature where the solutions are stirred with a magnetic stirrer (particularly since H_3PO_4 is inherently viscous). As in the wet etch for the GaAs/$Al_xGa_{1-x}As$ heterostructures, the wet etch is followed by two rounds of rinse in two separate petri dishes of deionized water and a final rinse in isopropanol. The sample is then left to dry in the hood.

---

* Extraneous glassware is removed from the hood as the HF fume will condense on the cool glass surfaces. All glassware in the hood are thoroughly rinsed after the experiments.

Chapter 4

Results and Discussion

The primary goal of this project is to demonstrate the ability to fabricate photonic bandgap bridge resonator structures out of both silicon and more important, III-V semiconductor material. To this end, scanning electron microscopic (SEM) images of the micromechanical structures represent the main presentation format of the results. In cases where free-standing structures are not attained, SEM images of the fabrication processes often reveals the reasons why they have not been successfully built. In this Chapter, the results and findings are presented for the various material systems employed.

4.1 Amorphous Si/SiO_2 Material System

As anticipated, the maturity of silicon technology produces Si/SiO_2 structures which present the more reliable and reproducible results in the project. The processes are well-controlled with the use of standard, characterized recipes in the Class 100 cleanroom environment of the ICL and TRL. Figure 4.1 illustrates free-standing 10 μm long bridges without any holes. Note the smoothness of the surfaces, a result of the excellent and reliable fabrication facilities available in the ICL and TRL. The beams are also relatively straight, thus implying that the inherent tensile stress in the amorphous silicon film is instrumental in this respect. Figure 4.2 shows another SEM photograph of a set of bridges without holes.

Figure 4.3 shows a 1 μm wide bridge which is 10 μm in length. Note the apparent transparency visible in part of the bridge, which is a result of the electrons penetrating that

portion of the beam. The actual width of the bridge is probably less than 1 μm as designed, particularly since a considerable amount of pattern fidelity has been lost when the photoresist mask is slightly etched during the RIE steps. Figure 4.4 shows a bridge that has buckled, presumably under its own weight. This bridge is 20 μm long and 1.5 μm wide by design. The buckling of the bridge illustrates the fundamental issue of mechanical soundness of the structures. In fact, while theoretical simulations of the resonators may yield structures with an optimized set of dimensions, the fundamental mechanical issues will introduce another limitation to the realization of the structures.

The importance of the mechanical issues become evident in Figure 4.5, where the SEM images of a set of collapsed structures can be seen. All the structures have invariably pinned to the substrate, with the defect region in the middle of the smaller bridges adhering to the substrate surface. One can imagine these bridge structures to be akin to a slab of material supported by two chains of the same material. The defect region material appears to have weighed down the two supporting links.

Figures 4.6 to 4.10 show some bridge structures with holes of different diameters and separations. It is observed that the longest bridges that remain standing are 30 μm in length, regardless of the width or type of hole configurations on the beam. Figures 4.11 and 4.12 illustrate some cantilever structures. Again, the cantilevers with lengths greater than 30 μm tend to droop and adhere to the substrate.

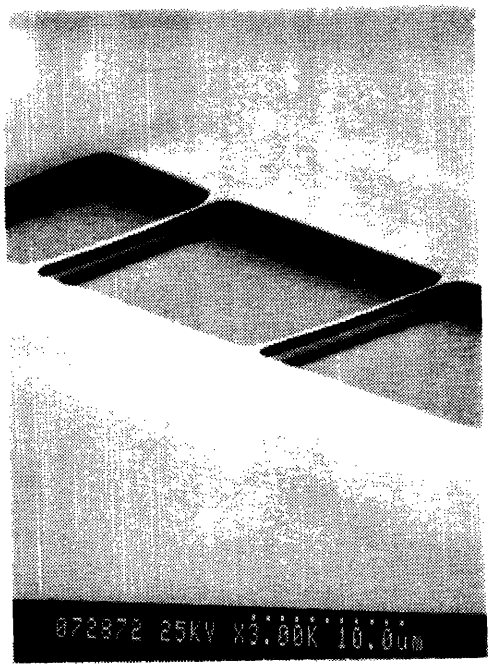

Figure 4.1: SEM photograph of bridge structures without hole. The bridges are 10 μm long; the structure in the foreground is 1.5 μm wide, while that in the background is 2 μm wide.

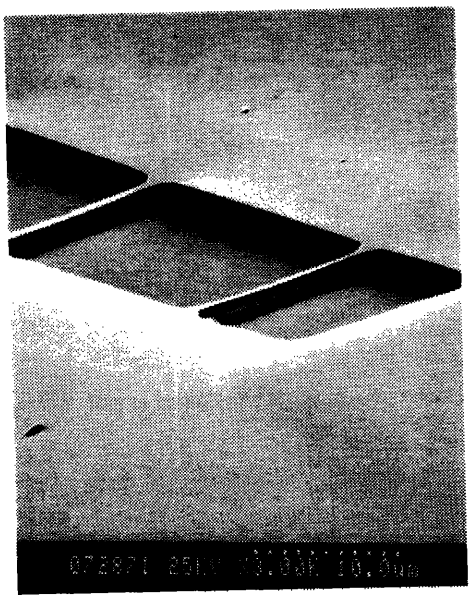

Figure 4.2: SEM photograph of bridge structures without holes. The bridges are 10 μm long; the structure in the foreground is 3 μm wide and that in the background is 4 μm wide.

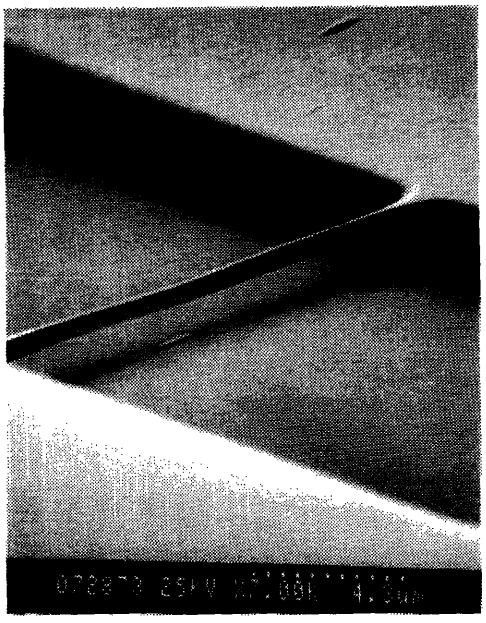

Figure 4.3: SEM photograph of a bridge structure that is 10 μm long and 1 μm wide (by design). Note the apparent transparency of a portion of the beam.

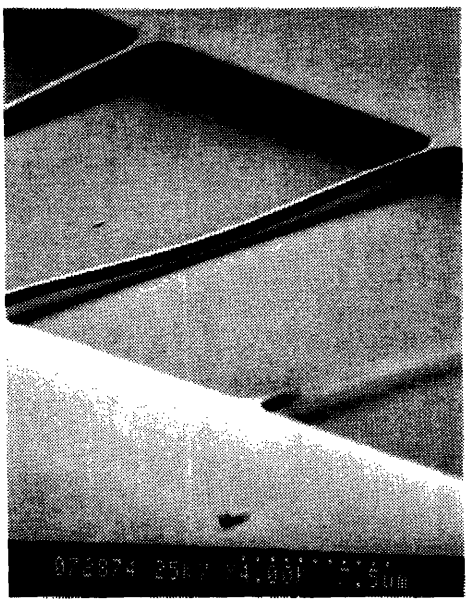

Figure 4.4: SEM photograph of a bridge structure which is 20 μm long and 4 μm wide. Note the buckling of the bridge, apparently under its own weight.

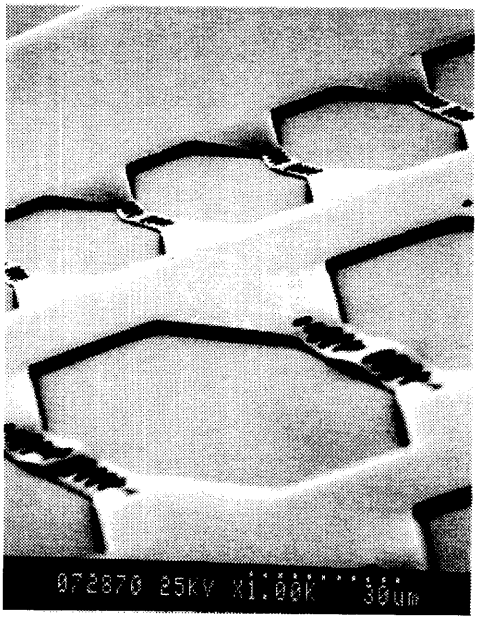

Figure 4.5: SEM photograph of collapsed bridge structures.

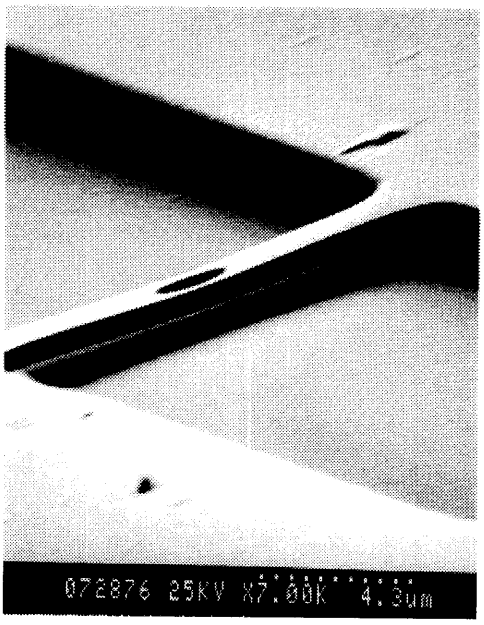

Figure 4.6: SEM photograph of bridge structure with a 2 μm diameter hole. The structure is 10 μm long and 3 μm wide.

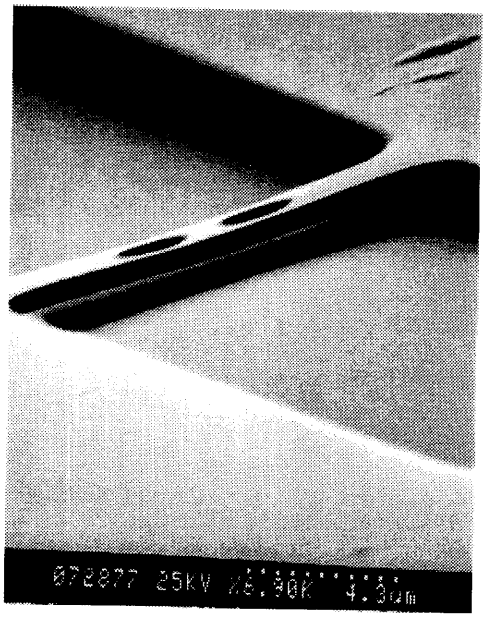

Figure 4.7: SEM photograph of bridge structure with 2 holes, each 2 μm in diameter and separated by 1 μm (side-to-side). The beam is 10 μm long and 3 μm wide.

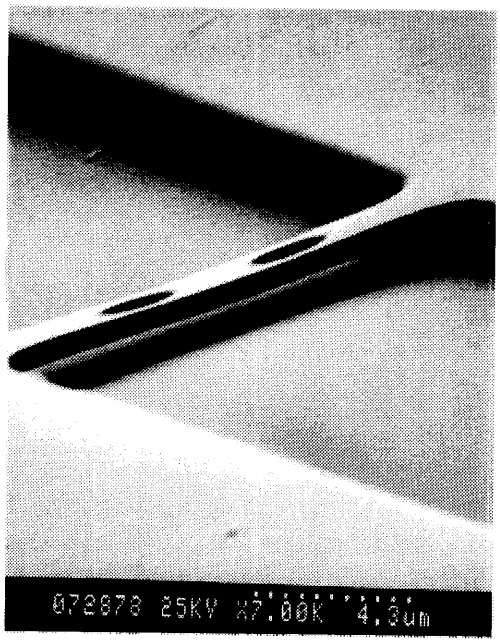

Figure 4.8: SEM photograph of bridge structure with 2 holes, each 2 μm in diameter and separated by 2 μm (side-to-side). The beam is 10 μm long and 3 μm wide.

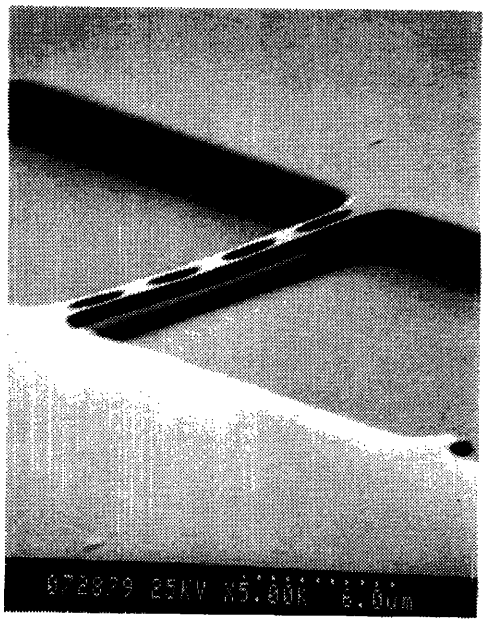

Figure 4.9: SEM photograph of bridge structure with 4 holes, each 2 μm in diameter and separated by 1 μm. The length of the bridge is 10 μm while its width is 4 μm.

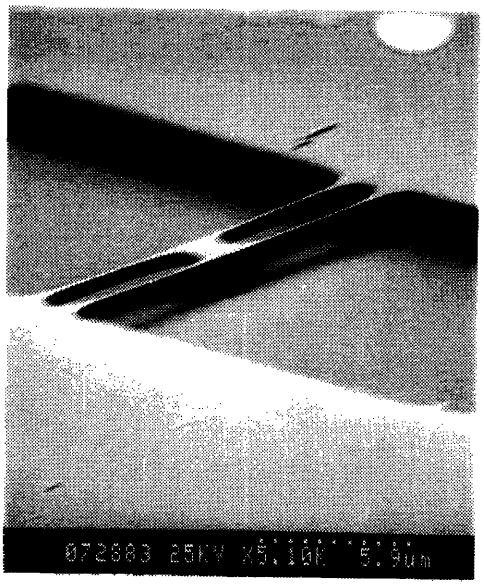

Figure 4.10: SEM photograph of bridge structure with 2 holes, each 3 μm in diameter and separated by 1 μm. The width of the beam is 4.5 μm and the length is 10 μm.

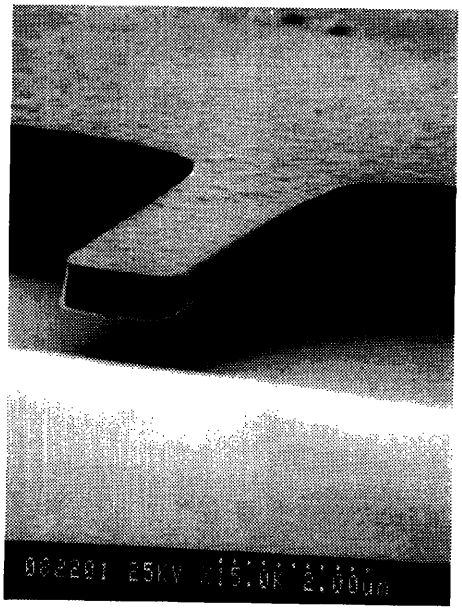

Figure 4.11: SEM photograph of a cantilever structure 10 μm long and 2 μm wide.

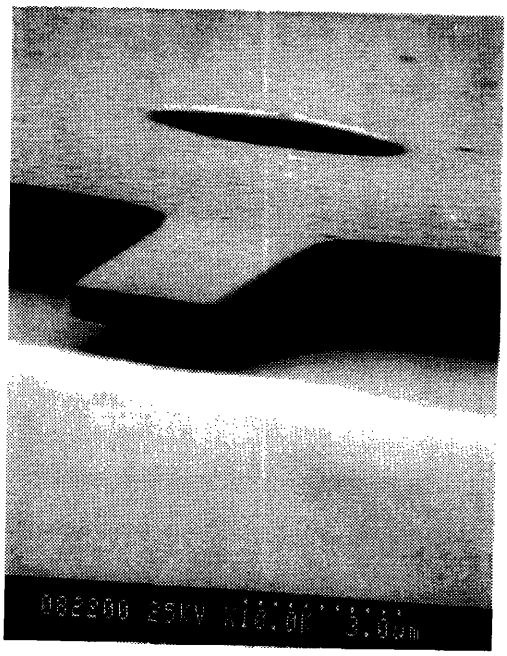

Figure 4.12: SEM photograph of a cantilever structure 10 μm long and 3 μm wide.

4.2 GaAs/$In_{0.5}Ga_{0.5}P$ Material System

In comparison to the amorphous Si/SiO_2 structures, the GaAs/$In_{0.5}Ga_{0.5}P$ heterostructures yield less satisfactory results. Specifically, the etchant used to remove the sacrificial layer in the GaAs/$In_{0.5}Ga_{0.5}P$ process has a practically negligible rate of undercutting the microstructures. The main structures that have been built successfully are the cantilever structures (Figures 4.13-4.14). In contrast, the bridge structures are not free standing as the sacrificial layer is not fully cleared (Figure 4.15). The drastic difference in the amount of undercut that has taken place is probably due to the fact that the etchant could reach the sacrificial layer in the cantilever structure via the tip. Nonetheless, one bridge structure was observed to have been free-standing (Figure 4.16).

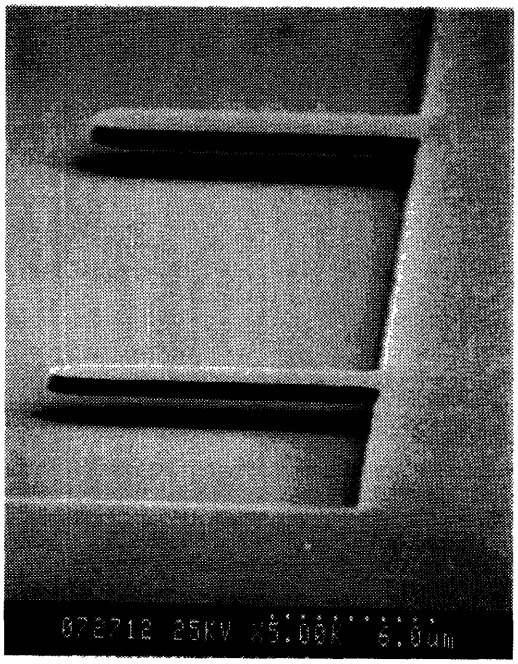

Figure 4.13: SEM photograph of GaAs/InGaP cantilever structures. The structures are both 10 μm long; the cantilever in the foreground is 2 μm wide, while that in the background is 3 μm wide.

Figure 4.14: SEM photograph of GaAs/InGaP cantilever structures. The structures are 20 μm long and the only free-standing structure is 4 μm wide.

4.3 GaAs/$Al_{0.3}Ga_{0.7}As$ Material System

As mentioned previously, the etchant used to remove the sacrificial layer in the GaAs/$Al_{0.3}Ga_{0.7}As$ heterostructure is far from ideal. Not only must the HF solution (the etchant) be warmed which results in the emission of a highly poisonous fume, the etching action is slow and leaves behind a relatively rough surface. The work on this material system, however, provides the motivation for working with a heterostructure with a higher Al content.

Figure 4.17 shows a bridge that has not been totally cleared, with a residual stump supporting the structure. Figure 4.18 provides a view of the roughness of the etched surface.

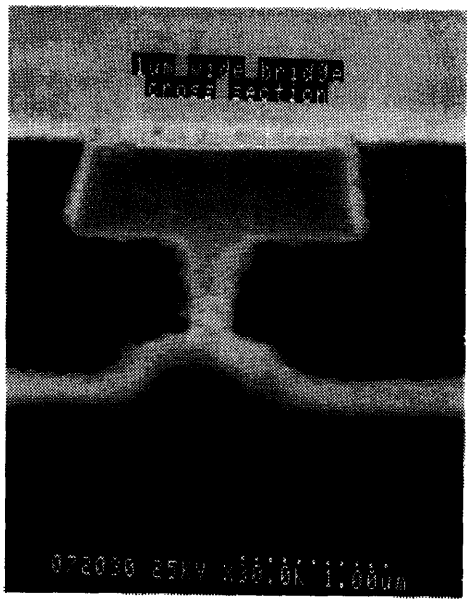

Figure 4.17: SEM photograph of the cross section of a 1 μm wide bridge. Note the stump underneath the beam which has not been cleared.

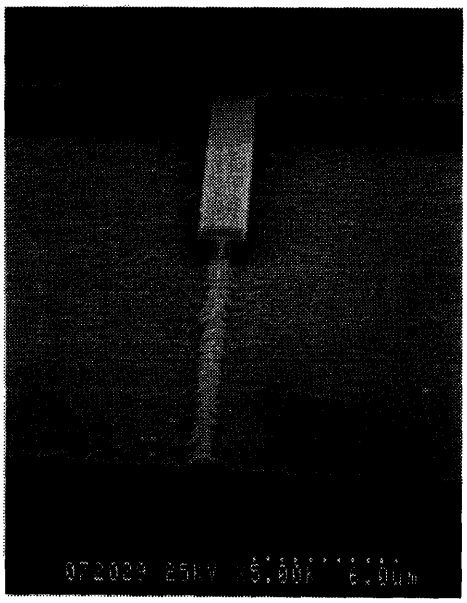

Figure 4.18: SEM photograph of the beam in Figure 4.17 at a higher magnification. Note the rough surface remaining after the wet etch.

4.4 GaAs/AlAs Material System

The experiments with the GaAs/AlAs material system are motivated by the difficulty encountered when using the GaAs/$Al_{0.3}Ga_{0.7}As$ heterostructure. The etching action of the HF solution on the sacrificial layer is expected to be much faster in the former than in the latter. In addition, the HF solution etches AlAs readily at room temperature, while it etches $Al_{0.3}Ga_{0.7}As$ at elevated temperature.

Amongst the III-V material systems that have been used in this project, the GaAs/AlAs material system yields a higher proportion of successful micromechanical structures. The quality of the structures, however, are not comparable with the amorphous Si/SiO_2 counterparts. In particular, the surface of the GaAs film that has had the underlying sacrificial material removed tend to buckle discernibly (see Figure 4.19).

Figure 4.20 illustrates the fundamental flaw of the design used for one of the structures. The amount of undercutting that has taken place on both ends of the beam is clearly visible leaving two triangle-shaped material remaining at either end. The support afforded by the two support seem insufficient to hold the beam up.

Figures 4.21 to 4.23 shows a series of bridges with various configurations of holes. The shadow cast by the beams clearly indicate that the holes have been etched through completely. Further, the etched surfaces, both on the substrate and on the beams themselves, appear to be smooth. In addition, the sidewalls of the bridges are sufficiently straight, a manifestation of the effectiveness of the RIE process.

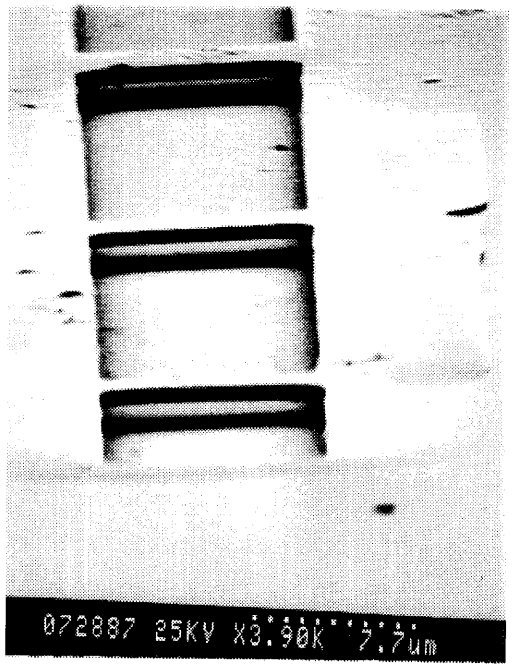

Figure 4.19: SEM photograph of GaAs/AlAs bridge structures without holes. Note the slightly raised surfaces on both ends of the beams which indicate the amount of undercutting that has taken place.

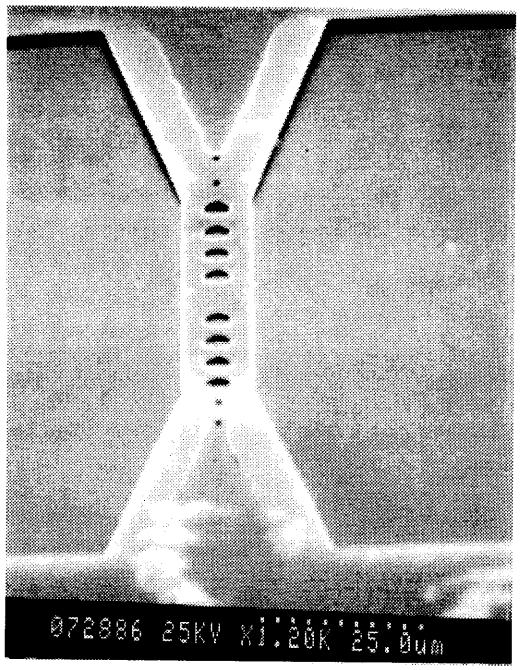

Figure 4.20: SEM photograph of a GaAs/AlAs bridge structure which is pinned to the substrate. The margins visible along the edges of the structure arise from the undercutting that has taken place.

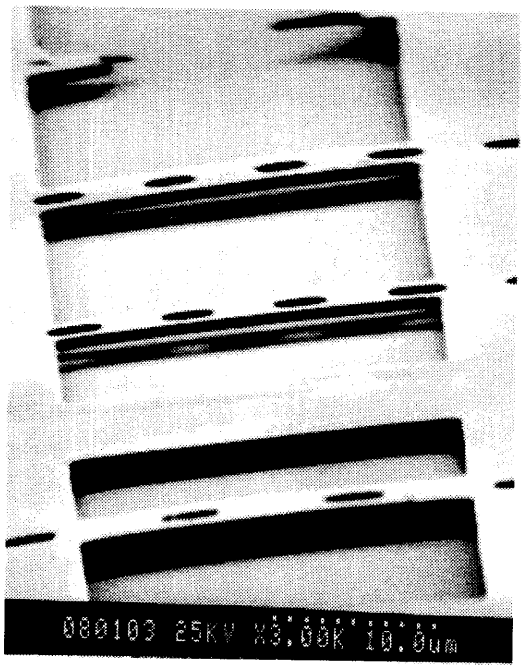

Figure 4.21: SEM photograph of GaAs/AlAs bridge structures. The bridges are all 20 μm long and the holes are 2.5 μm in diameter. The widths range from 3.5 to 5.5 μm.

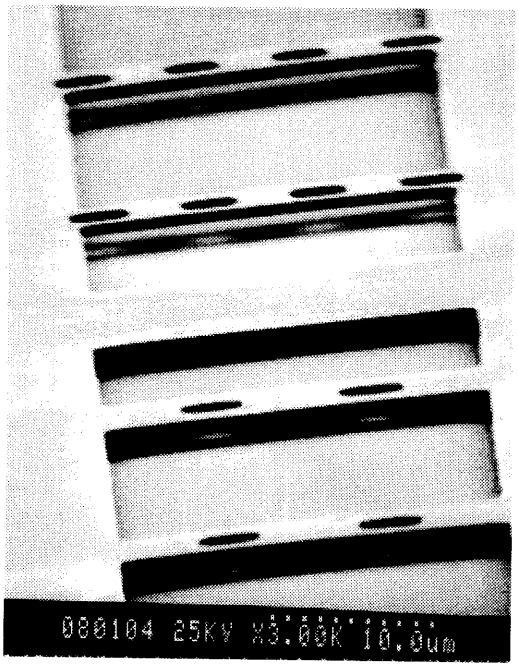

Figure 4.22: SEM photograph of GaAs/AlAs bridge structures. The physical dimensions of the structures are similar to those in Figure 4.21.

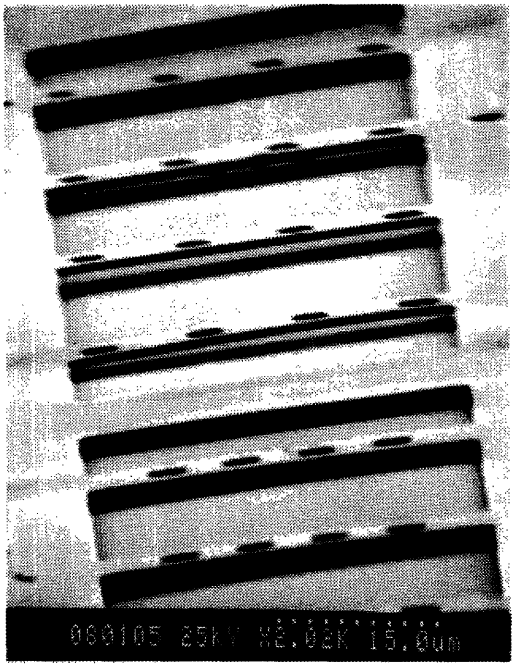

Figure 4.23: SEM photograph of GaAs/AlAs bridge structures. The structures are all 30 μm long and the holes are all 3 μm in diameter. The widths of the structures range from 4 to 7 μm.

Chapter 5

Conclusion

In summary, micromechanical bridge resonator structures have been fabricated with both Si/SiO_2 and III-V material systems. Various configurations of these bridges, consisting of different dimensions and number of holes along the beam, have been built. These bridges can potentially be used as photonic band gap bridge resonators which in turn, have immense promise in the introduction of a new class of photonic devices. Other micromechanical features like the cantilevers have also been fabricated with both types of material systems.

In the process of building these devices, various fabrication issues have been investigated and addressed. Particularly salient in this respect are the process steps for the III-V material. First, the composition of the heterostructure has been varied to provide an idea of the easier combination to employ from the process standpoint. The process characteristics for the fabrication of various III-V heterostructures have also been established, and the idiosyncrasies pertaining to each material system have been recorded. In particular, the appropriate RIE and wet etch parameters have been investigated to provide a viable and reproducible way of fabricating these devices. In addition, device dimensions approaching the limits of optical lithography have been attained.

Apart from the fabrication process, the mechanical issues involved in fabricating these micromechanical structures have also been highlighted. For instance, a tensile amorphous silicon film yields positive results, where a compressive polysilicon film fails to produce free-standing structures. Stress measurements have been conducted to verify that the residual stress in the amorphous silicon film is indeed tensile in nature. Furthermore,

the failure of certain device designs has brought to light the importance of the structural integrity of the essentially mechanical structures.

The free-standing structures arising from this effort have brought not only immense satisfaction, but they have also provided the impetus for future work. Looking ahead, the next step will be the optical testing of these devices to establish the physical phenomenon that computer simulations have demonstrated. The optical testing will likely involve the propagation of electromagnetic radiation along the devices which, in turn, introduces other challenges. For instance, the reflection of the electromagnetic waves at the edge of the devices will need to be addressed. Should the outcome be positive, nonetheless, the ultimate goal will be the introduction of an active region into the defect region. By introducing a practical dimension to the physically interesting effect, it is hoped that the devices will take on an important role in both the research and the commercial community.

Along the path to the ultimate goal, several issues will have to be addressed. Broadly, these issues can be classified as either fabrication or mechanical problems. In the fabrication sequence, novel techniques will have to be employed to attain smaller device sizes beyond the limits of optical lithography. In particular, resonators operating in the regime of 1.55 μm wavelength may require features to be as small as 0.4 μm[13]. Increasingly sophisticated processes will then need to be devised to optimize the structures. Also, as different material systems may have to be used, possibly whole new sets of process parameters will need to be investigated.

As mentioned previously, not all mechanical designs conceived are structurally sound. Consequently, some form of mechanical simulations will have to be incorporated in tandem with the purely electromagnetic simulations. In addition, the mechanical properties of the III-V material will need to be better understood, though work in this regard is already underway elsewhere[35,36].

All in all, the progress in the field of photonic band gap devices has been exciting and promises to be so in the future. Hopefully, this project will provide a launching pad

for more exciting results and deeper understanding of the intrinsically intriguing physical phenomenon.

Appendix A

The layout of the mask is shown in Figure A-1 while Figure A-2 represents a categorization of the various features on the mask. The various categories of structures are described as follows:

a) These micromechanical bridges, illustrated by Figure A-3, are as derived from Reference 21. There are in total five rows of these bridges with eight holes each (four on each side of the defect region), scaled by approximately twofolds in the dimensions between adjacent rows. The dimensions of the relevant features are summarized in Table A-1:

	Width of Bridge, W (μm)	Length of Bridge, L (μm)	Approx.Hole Diameter,d (μm)	Hole Separation,S (μm)	Width of Defect Region, D (μm)
Row 1	4.2	33.0	2.5	1.0	4.5
Row 2	8.5	68.5	5.2	2.0	9.0
Row 3	12.8	98.0	7.8	3.0	13.8
Row 4	17.0	130.0	10.6	4.0	18.2
Row 5	21.5	160.0	13.2	5.0	22.6

Table A-1: Physical features dimensions of structures in Zone A.

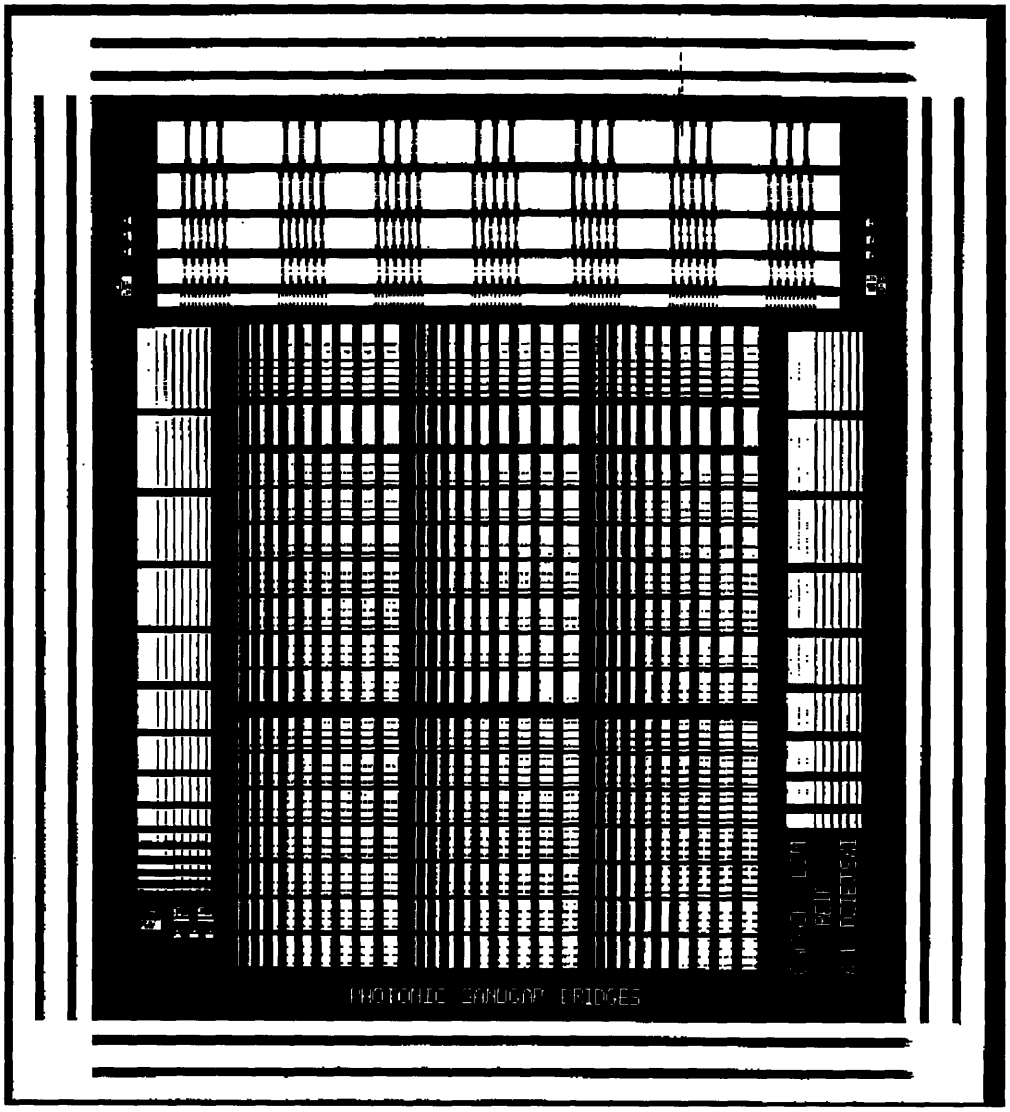

Figure A-1: A macroscopic view of the layout of the mask.

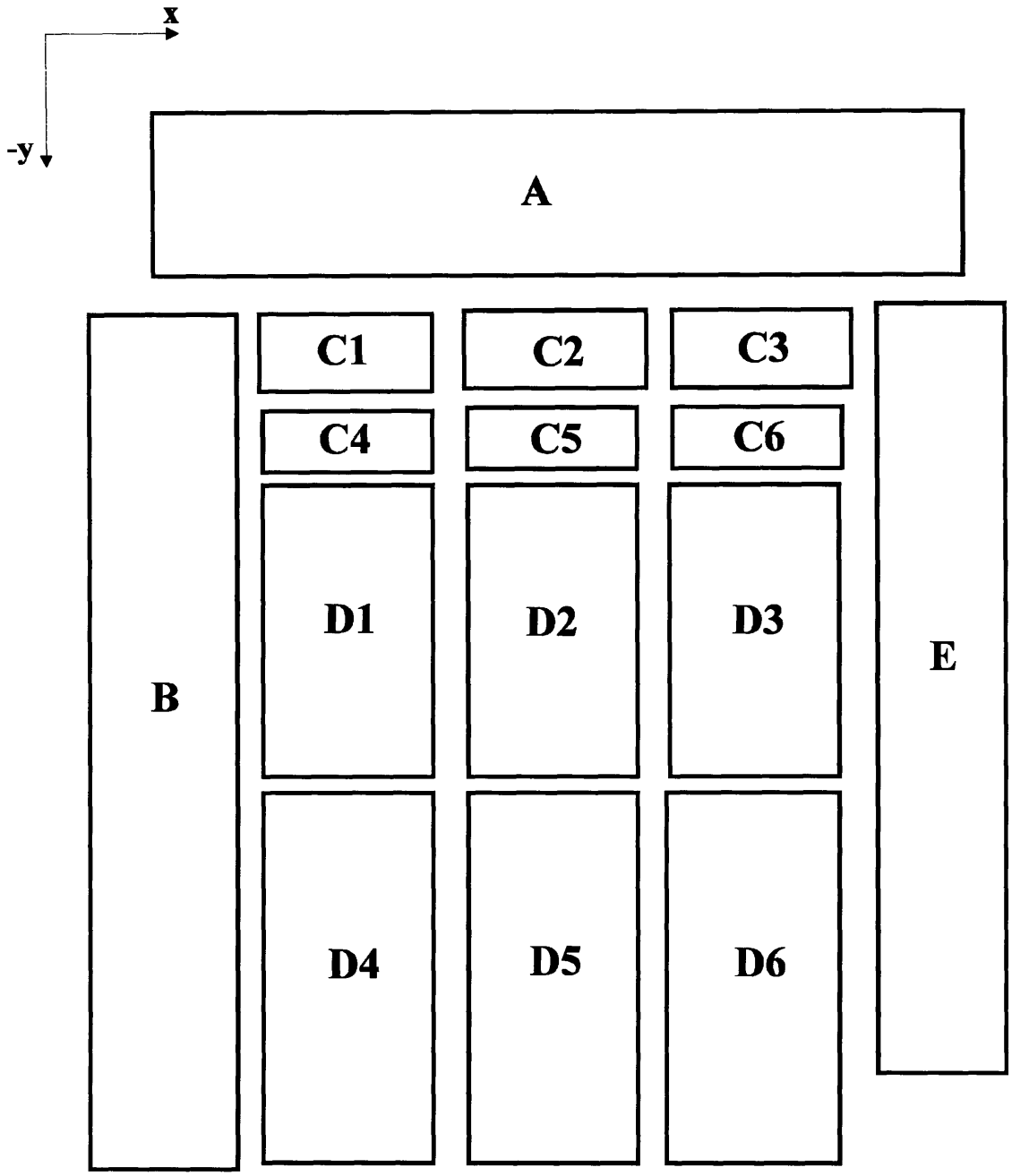

Figure A-2: Categorization of the various micromechanical features on the mask.

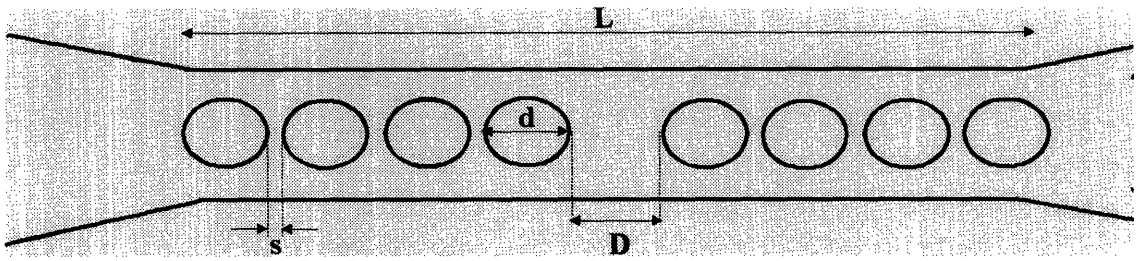

Figure A-3: The photonic bandgap bridge structure in zone A.

b) **Zone B**: This category of micromechanical structures consist of 7 groups of cantilevers. The length of the cantilevers varies between groups from 10 to 50 μm, in increment of 10 μm, and from 100 to 300 μm, in steps of 50 μm. Within each group of a constant length, the width of the cantilevers range from 2 to 10 μm, in steps of 1 μm (see Figure A-4).

c) **Zone C**: This zone consists of 6 separate groups of micromechanical bridges without holes. In subzone C1, the length of the bridges range from 10 to 100 μm in steps of 10 μm in the x direction (as marked in Figure A-2), while the width of the bridges range from 2 to 10 μm in steps of 1 μm in the -y direction. Subzones C2 and C3 have the same structures as C1. In subzone C4, the length of the bridges are 0.5 μm, 0.7 μm, 1.0 μm, 1.5 μm and 2.0 μm respectively; the width of the bridges range from 10 to 100 μm in steps of 10 μm. Subzones C5 and C6 mimics the pattern in C4.

d) **Zone D**: The structures in this zone consist of micromechanical bridges with holes placed in a periodic fashion along the beams in different ways. The zone can further be subdivided into six main clusters, with holes of different diameters in each subzone. In

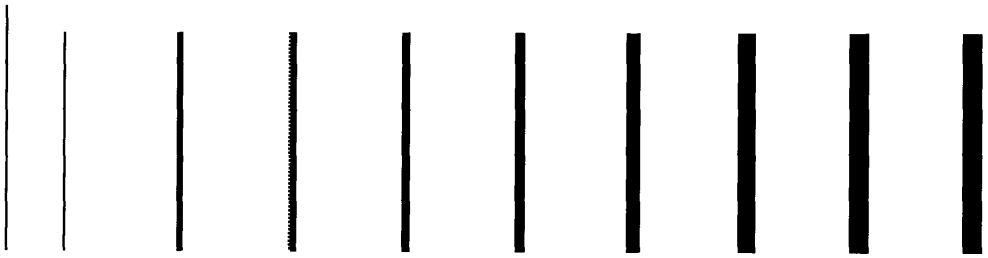

Figure A-4: Micromechanical cantilever structures in a group of constant length. The width of the cantilevers range from 2 μm to 10 μm, in steps of 1 μm from left to right.

subzone D1, the holes are all 1 μm in diameter. Within the subzone, the bridges range from 10 to 100 μm in the x-direction. In the -y direction within the subzone, there are seven sets of bridges all with widths ranging from 3 to 6 μm in steps of 1 μm. These sets of bridges have different number of holes and different hole-to-hole separation: (a) 1 hole in the middle of the beam; (b) 2 holes separated by 1 μm; (c) 2 holes separated by 2 μm; (d) 4 holes separated by 1 μm; (e) 4 holes separated by 2 μm; (f) 8 holes separated by 1 μm; and (g) 8 holes separated by 2 μm.

In subzone D2, the holes are all 1 μm in diameter. Again, the bridges range from 10 to 100 μm in length by steps of 10 μm in the x direction. In the -y direction within the subzone, there are seven sets of bridges all with widths ranging from 2 to 5 μm in steps of 1 μm. These sets of bridges have different number of holes and different hole-to-hole separation: (a) 1 hole in the middle of the beam; (b) 2 holes separated by 1 μm; (c) 2 holes separated by 2 μm; (d) 4 holes separated by 1 μm; (e) 4 holes separated by 2 μm; (f) 8 holes separated by 1 μm; and (g) 8 holes separated by 2 μm.

In subzone D3, the holes are all 1.5 μm in diameter. In the x-direction, the bridges range 10 to 100 μm in length by steps of 10 μm. In the -y direction within the subzone, there are seven sets of bridges all with widths ranging from 2.5 to 5.5 μm in steps of 1 μm. These sets of bridges have different number of holes and different hole-to-hole separation: (a) 1 hole in the middle of the beam; (b) 2 holes separated by 1 μm; (c) 2 holes separated by 2 μm; (d) 4 holes separated by 1 μm; (e) 4 holes separated by 2 μm; (f) 8 holes separated by 1 μm; and (g) 8 holes separated by 2 μm.

In subzone D4, the holes are all 2.5 μm in diameter. In the x-direction, the bridges range 10 to 100 μm in length by steps of 10 μm. In the -y direction within the subzone, there are seven sets of bridges all with widths ranging from 3.5 to 6.5 μm in steps of 1 μm. These sets of bridges have different number of holes and different hole-to-hole separation: (a) 1 hole in the middle of the beam; (b) 2 holes separated by 1 μm; (c) 2 holes separated by 2.5 μm; (d) 4 holes separated by 1 μm; (e) 4 holes separated by 2.5 μm; (f) 8 holes separated by 1 μm; and (g) 8 holes separated by 2.5 μm.

In subzone D5, the holes are all 3.0 μm in diameter. In the x-direction, the bridges range 10 to 100 μm in length by steps of 10 μm. In the -y direction within the subzone, there are seven sets of bridges all with widths ranging from 4 to 7 μm in steps of 1 μm. These sets of bridges have different number of holes and different hole-to-hole separation: (a) 1 hole in the middle of the beam; (b) 2 holes separated by 1 μm; (c) 2 holes separated by 3 μm; (d) 4 holes separated by 1 μm; (e) 4 holes separated by 3 μm; (f) 8 holes separated by 1 μm; and (g) 8 holes separated by 3 μm.

In subzone D6, the holes are all 4 μm in diameter. In the x-direction, the bridges range 10 to 100 μm in length by steps of 10 μm. In the -y direction within the subzone, there are seven sets of bridges all with widths ranging from 5 to 8 μm in steps of 1 μm. These sets of bridges have different number of holes and different hole-to-hole separation: (a) 1 hole in the middle of the beam; (b) 2 holes separated by 1 μm; (c) 2 holes separated by 4 μm; (d) 4 holes separated by 1 μm; (e) 4 holes separated by 4 μm; (f) 8 holes separated by 1 μm; and (g) 8 holes separated by 4 μm.

e) **Zone E**: The structures in this zone consist of long bridges with lengths varying from 100 to 500 μm in steps of 50 μm in the +y direction. Within a group of bridges with constant length, the width ranges from 2 to 10 μm in steps of 1 μm in the x direction.

Appendix B

Results from RIE and Wet Etch of III-V Materials

The etch rates of the various RIE steps for the different material are determined by profilometric measurements before and after the fact. In addition, the SEM images taken of the samples after the wet etch sequence also reveal the morphology of the surfaces after the etch. The following sections summarize the results for the three different kinds of material systems that have been used.

B.1 GaAs/$Al_{0.3}Ga_{0.7}As$

B.1.1 RIE

(a) Before the RIE etch, the thickness of the photoresist (PR) is measured, at a step feature on the sample to be: $h_1 = 1.11$ μm.

(b) After a 4 minute etch in the $SiCl_4/BCl_3$ gas discharge as described in Section 3.2.2, the step height is measured to be: $h_2 = 1.73$ μm. Hence, $\Delta h = (1.73\text{-}1.11)$ μm = 0.62 μm. Of the 0.62 μm thickness of material removed, 0.5 μm consists of the top GaAs layer.

(c) The PR was removed and the step height measured again to yield: $h_3 = 0.81$ μm. This implies that the amount of PR left after the RIE step is: $t_{PR} = (1.73\text{-}0.81)$ μm = 0.92 μm. Consequently, the amount of PR that has been etched in 4 minutes is: $\Delta t_{PR} = h_1\text{-}t_{PR} = (1.11\text{-}0.92)$ μm = 0.29 μm. Hence, the etch rate for the PR is calculated to be 725 Å/min.

(d) At the same time, 0.50 μm of GaAs and 0.31 μm of $Al_{0.3}Ga_{0.7}As$ have been etched in 4 minutes. However, by assuming the etch rate of GaAs to be approximately 2500 Å/min

(as obtained in a separate etch characterization experiment), the etch rate for $Al_{0.3}Ga_{0.7}As$ is estimated to be 1600 Å/min.

B.1.2 Wet Etch

After etching the samples in warmed HF for 10 minutes, the step height is measured to be 1.47 μm. Further etching yields no change in step height, thus implying that the wet etch has stopped on the substrate. As a result, the *lower bound* of the etch rate of $Al_{0.3}Ga_{0.7}As$ in warmed HF is: (1.47-0.81) μm/10 min = 660 Å/min. The etch rate is, nonetheless, expected to be faster than the above.

However, the SEM images revealed that the sacrificial layer has not been totally removed (see Figure B.1). In fact, the morphology of the etched surface appears relatively rough as illustrated in Figure B.2. Interestingly, there is an apparent crystallographic preference in the etch characteristic as revealed in Figure B.3. At this juncture, no further experiment is conducted with the heterostructure due to a shortage of the material. The GaAs/AlAs material system is used instead which yields better results.

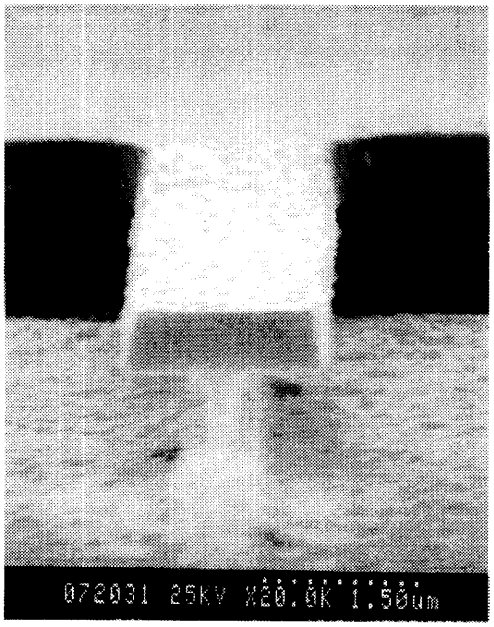

Figure B.1: Cross-sectional view of a cleaved beam. Note that the sacrificial layer is not totally cleared and that the etched surfaces are relatively rough.

Figure B.2: Morphology of the etched surfaces. The roughness on the surface of the sacrificial layer under the beam is visible.

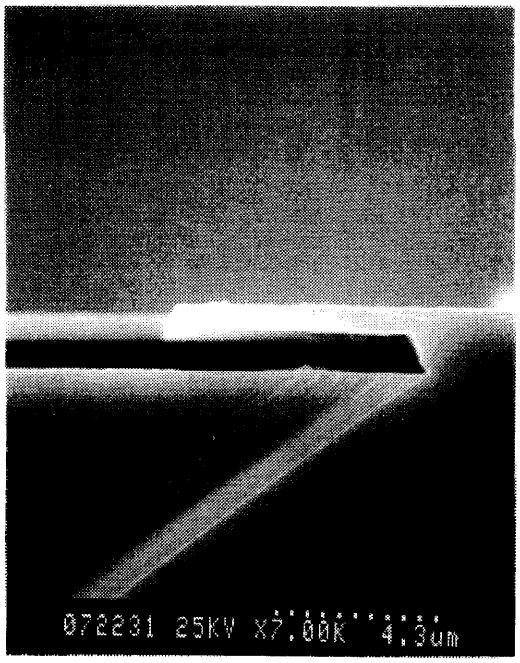

Figure B.3: A side view of the etch front. The preference of the etching action for a certain crystallographic direction is apparent.

B.2 GaAs/AlAs

B.2.1 RIE

(a) Before the etch, the PR thickness on a step feature is measured to be: $h_1 = 1.10$ μm.

(b) After an etch with $SiCl_4/BCl_3$ for 4 minutes, the step height is measured to be: h2 = 1.82 μm.

(c) After the PR has been removed, the step height is measured to be: $h_3 = 0.87$ μm. Therefore, the PR thickness after the RIE is: $\Delta h = h_3 - h_2 = (1.82-0.87)$ μm = 0.95 μm. The amount of PR that has been removed in 4 minutes of etch is: (1.10-0.95) μm = 0.15 μm. Consequently, the etch rate for PR in this experiment is: 0.15 μm/4 min = 375 Å/min. This is about half the rate obtained in Section B.1. The discrepancy is probably due to the different condition (for instance, humidity, temperature etc.) under which the resist has been processed. Nonetheless, the discrepancy is not critical to the overall process.

The amount of GaAs/AlAs material that has been etched thus far is 0.87 μm. Of this amount, 0.5 μm consists of GaAs and 0.37 μm is AlAs. Assuming the etch rate of GaAs to be 2500 Å/min, the etch rate for AlAs is: 0.37 μm/4 min = 925 Å/min. Figure B.5 shows an optical micrograph of the sample after the RIE step. Note the distinct globular features on the etched surface, which is probably due to the fact that AlAs becomes rapidly oxidized when exposed to air. The non-uniformity in oxidation has thus resulted in the rough surface morphology.

B.2.2 Wet Etch

The wet etch of the GaAs/AlAs heterostructure is particularly rigorous, even in a diluted HF solution. The nominal etch rate of 20:1 H_2O:HF on AlAs is estimated to be: (1.50-0.37) μm/0.5 min = 2.26 μm/min. Of course, the etch rate is probably much faster than the above figure, given the rapid etching action of the solution.

Figure B.5 shows the morphology of the sample after the wet etch. Note that the etched surface is relatively smooth. However, the top GaAs surface appears wrinkled, probably due to the fact that the etch is so intense with a great amount of bubbling. This phenomenon may also be a result of the oxidation of the sacrificial AlAs layer, which alters the initial lattice-matched, stress-free condition of the GaAs/AlAs interface.

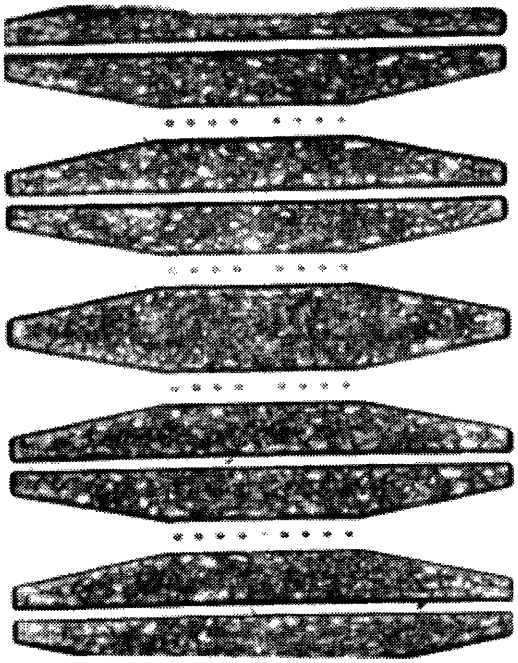

Figure B.4: Nomarski microscope photograph of the sample after the RIE sequence. Note the roughness of the etched regions between the bridge structure, which is due to the oxidation of the AlAs material when exposed to air.

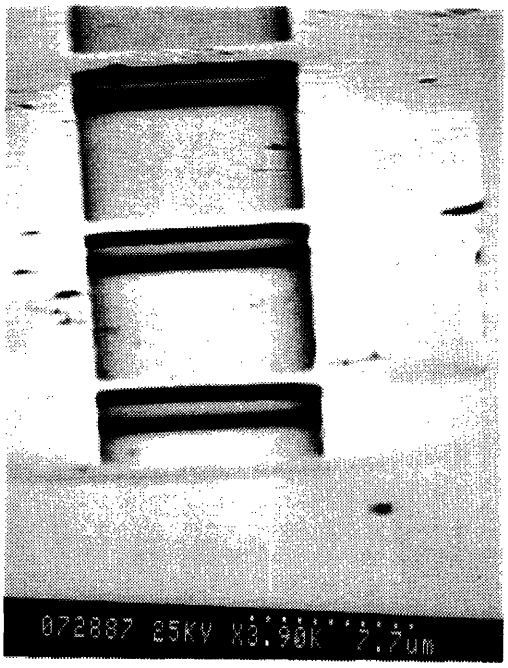

Figure B.5: SEM micrograph of bridge structures. The uneven surfaces on the ends of the beams reveal the amount of undercutting that has taken place.

B.3 GaAs/$In_{0.5}Ga_{0.5}P$

B.3.1 RIE

(a) The PR thickness on a step feature is first measured to be: h_1 = 1.18 μm.

(b) After an RIE etch with $SiCl_4/BCl_3$ for 1.8 min, the step height is measured to be: h_2 = 1.58 μm. Hence, the change in step height is: Δh = (1.58-1.18) μm = 0.40 μm. Assuming that the amount of PR that has been etched away is negligible and that the change in step height is purely due to the removal of III-V material, the etch rate for the GaAs top layer is estimated to be: 0.40 μm/1.8 min = 2200 Å/min.

(c) The sample is then subjected to an RIE step with CH_4/H_2 for 20 minutes. After the PR has been stripped, the step height is measured to be: h_3 = 0.65 μm with a distinct layer of residue left on the surface of the sample. As data pertaining to the etch rate of GaAs in CH_4/H_2 is unavailable, the etch rate of $In_{0.5}Ga_{0.5}P$ in the same gases cannot be inferred. Nonetheless, the fact that $In_{0.5}Ga_{0.5}P$ is etched at all implies that the scheme of stopping the chlorine-based etch before the $In_{0.5}Ga_{0.5}P$ layer has succeeded.

B.3.2 Wet Etch

The wet etch using the H_3PO_4/HCl mixture of varying proportions have yielded the same results. Specifically, while the etch rate in the normal direction to the sample has proceeded as expected (as measured by step profilometry before and after the etch), the etch in the directions transverse to the plane of the sample has been obstinately slow. In fact, even an extended etch period of more than 2 hours with the various mixtures fails to produce any significant undercut. It is speculated that there exists very strong crystallographic preferences of the etchant on $In_{0.5}Ga_{0.5}P$, as revealed in Figure B.6. Further, a number of irregular features tend to exist on the etched surfaces (Figure B.7).

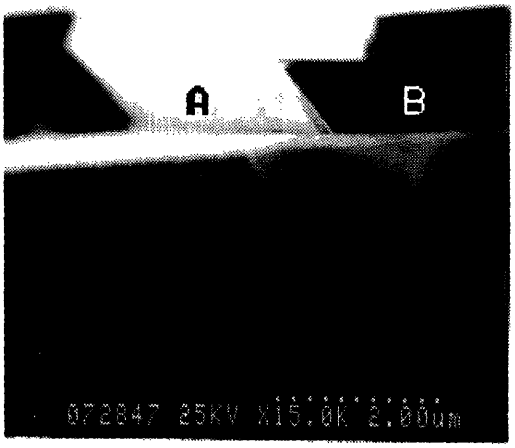

Figure B.6: SEM photograph of two perpendicular etch fronts (marked as A and B). Note the distinctly different angles at which the two fronts seem to have proceeded.

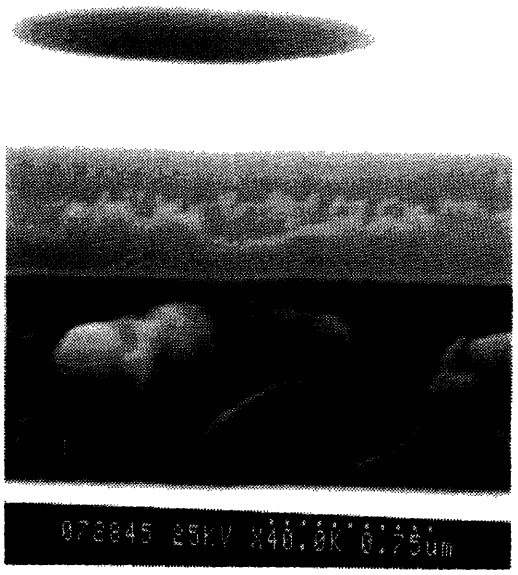

Figure B.7: SEM photograph of the etched surface of an uncleared sacrificial layer. The irregular features on the surface can be easily seen. This sample has been etched for two hours in a 1:1 H_3PO_4/HCl etchant.

References

[1]E. Yablonivitch. *Inhibited Spontaneous Emission in Solid-State Physics and Electronics.* Phys. Rev. Lett. Vol. 58 No.20 pp 2059 (1987).

[2]S. John. *Strong Localization of Photons in Certain Disordered Superlattices.* Phys. Rev. Lett. Vol. 58 No. 23 pp 2486 (1987).

[3]E. Yablonovitch and T.J. Gmitter. *Photonic Band Structure: The Face-Centered-Cubic Case.* Phys. Rev. Lett. Vol. 63 No. 18 pp 1950 (1989).

[4]K.M. Ho, C.T. Chan, and C.M. Soukoulis. *Existence of a Photonic Gap in Periodic Dielectric Structures.* Phys. Rev. Lett. vol. 65 no. 25 pp 3152 (1990).

[5]K.M. Leung and Y.F. Liu. *Full Vector Wave Calculation of Photonic Band Structures in Face-Centered-Cubic Dielectric Media.* Phys. Rev. Lett. Vol. 65 No. 21 pp 2646 (1990).

[6]Z. Zhang and S. Satpathy. *Electromagnetic Wave Propagation in Periodic Structures: Bloch Wave Solutions of Maxwell's Equations.* Phys. Rev. Lett. Vol. 65 No. 21 pp 2650 (1990).

[7]W.M. Robertson, G. Arjavalingam, R.D. Meade, K.D. Brommer, A.M. Rappe and J.D. Joannopoulos. *Measurement of Photonic Band Structure in a Two-Dimensional Periodic Dielectric Array.* Phys. Rev. Lett. Vol. 68 No. 13 pp 2023 (1992).

[8]E. Yablonovitch, T.J. Gmitter, R.D. Meade, A.M. Rappe, K.D. Brommer and J.D. Joannopoulos. *Donor and Acceptor Modes in Photonic Band Structure.* Phys. Rev. Lett. Vol. 67 No. 24 pp 3380 (1991).

[9]E. Yablonovitch. *Photonic Band-Gap Structures.* J. Opt. Soc. Am. B. Vol. 10 No. 2 pp 283 (1993).

[10] K.M. Ho, C.T. Chan, C.M. Soukoulis, R. Biswas and M. Sigalas. *Photonic Bandgaps in Three Dimensions: New Layer-by-layer Periodic Structures.* Solid State Communications. Vol. 89 No. 5 pp. 413-416 (1994).

[11] J.R. Wendt, G.A. Vawter, P.L. Gourey, T.M. Brennan and B.E. Hammons. *Nanofabrication of Photonic Lattice Structures in GaAs/AlGaAs.* J. Vac. Sci. Technol. B Vol. 11 No. 6 pp. 2637 (1993).

[12] Dr. Pierre R. Villeneuve, private conversation.

[13] S. Fan, J.N. Winn, A. Devenyi, R.D. Meade and J.D. Joannopoulos. *Guided and Defect Modes in Periodic Dielectric Waveguides.* To be published in J. Opt. Soc. Am. B.

[14] B.S. Meyerson, F.J. Himpsel, and K.J. Uram. Bistable conditions for low-temperature silicon epitaxy. Appl. Phys. Lett. Vol. 57, No. 10, pp. 1034, 3 Sept 1994.

[15] Charles Hsu, private conversation.

[16] P. Krulevitch. *Growth Stresses in Undoped LPCVD Polycrystalline Silicon Films.* Master of Engineering Thesis, University of California, Berkeley. May, 1991.

[17] D-G Oei and S.L. McCarthy. *The Effect of Temperature and Pressure on Residual Stress in LPCVD Polysilicon Films.* Ford Motors Inc. Internal Report.

[18]Charles Hsu, private conversation. The "590°C Recipe" in the TRL is developed by Charles Hsu in conjunction with Nestor Polce.

[19] S. Wolf and R.N. Tauber. Silicon Processing for the VLSI Era, Volume 1. pp117. Lattice Press, 1986.

[20] R.W. Hoffman. *Mechanical Properties of Thin Condensed Films.* Physics of Thin Films, Vol. 3, ed. by G. Hass and T.E. Thun. pp. 211, Academic Press, New York, 1966.

[21] Prof. John D. Joannopoulos, Dr. Pierre R. Villeneuve and S. Fan. Private conversations.

[22] C.H. Mastrangelo and C.H. Hsu. *Mechanical Stability and Adhesion of Microstructures Under Capillary Forces -- Parts I and II.* IEEE Journal of Microelectromechanical Systems, Vol. 2, No. 1, pp 33-55, March 1993.

[23] E.W. Flosdorf. *Freeze Drying: Drying by Sublimation.* University Microfilms International, Ann Arbor, MI, 1982.

[24] N. Takeshima, K.J. Gabriel, M. Ozaki, J. Takahashi, H. Horiguchi and H. Fujita. *Electrostatic Parallelogram Actuators.* Tranducers '91. pp 63-66, 1991.

[25] K. Lu. *Lattice-Matched (In,Ga)P Buffer Layers for ZnSe Based Visible Emitters.* Master of Science Thesis, Massachusetts Institute of Technology, February 1994.

[26] J.L. House. *Optical Characterization of ZnSe by Photoluminescence.* Master of Science Thesis, Massachusetts Institute of Technology, February 1994.

[27] S.J. Pearton. *Dry Etching Techniques and Chemistries for III-V Semiconductor.* Mat. Res. Soc. Sym. Proc. Vol. 216 pp 277, 1991.

[28] D.G. Lishan and E.L. Hu. *Chlorine and HCl Radical Beam Etching of III-V Semiconductors.* J. Vac. Sci. Technol. B Vol. 8, No. 6, pp. 1951, 1990.